J. Fluid Mech. (2003), *vol.* 497, *pp.* 67–98.
DOI: 10.1017/S0022112003006591 Printed in the United Kingdom

Secondary Kelvin–Helmholtz instability in weakly stratified shear flow

By WILLIAM D. SMYTH

College of Oceanic and Atmospheric Sciences, Oregon State University, Corvallis, OR 97331, USA

(Received 27 January 2003 and in revised form 24 July 2003)

The growth of secondary vortices on the braids separating Kelvin–Helmholtz billows is investigated via numerical simulations. The similarity theory of Corcos & Sherman (1976) is extended to include mixing processes with Prandtl number greater than unity, and is shown to provide a useful description of the physics of the braid regions just prior to the onset of secondary instability. The numerical study of Staquet (1995) is extended to include a wider range of Prandtl numbers and bulk Richardson numbers. Length and time scales of the secondary instability are compared with predictions based on normal-mode stability analysis of the braids. The onset of instability is shown to be accompanied by a dramatic increase in mixing efficiency in the braid region, emphasizing the potential importance of preturbulent Kelvin–Helmholtz billows for mixing stratified fluids.

1. Introduction

In many fluid systems, turbulence and mixing are governed by a competition between large-scale shear and stable ambient density stratification. Kelvin–Helmholtz (KH) instability of a stratified, parallel shear layer has been a standard model for this class of flows since it was first described by Kelvin (1871). Recently, direct numerical simulation (DNS) studies have added considerably to our understanding of this instability and of the large-amplitude billows that emerge as a result (e.g. Caulfield & Peltier 1994; Cortesi, Yadigaroglu & Banerjee 1998; Smyth 1999; Cortesi *et al.* 1999; Smyth & Moum 2000*a*, *b*; Caulfield & Peltier 2000; Staquet 2000; Smyth, Moum & Caldwell 2001). Of particular interest here is the discovery that the mixing efficiency of KH billows is extraordinarily high in the preturbulent phase, then relaxes to the canonical value of 0.2 after turbulence develops (e.g. Winters *et al.* 1995; Smyth & Moum 2000*b*; Caulfield & Peltier 2000; Staquet 2000; Smyth *et al.* 2001; Staquet & Bouruet-Aubertot 2001). In a typical DNS of a turbulent event driven by KH instability, the preturbulent phase accounted for 1/4 of the net potential energy gain (Smyth *et al.* 2001). This highly efficient mixing occurs largely in the braids, regions of intense property gradients that separate individual billows.

Braids are regions of strongly sheared, nearly parallel flow, and thus have the potential to develop secondary KH instability. Corcos & Sherman (1976) developed a similarity theory for the braids and thereby predicted that the Richardson number characterizing the stability of the braids would be inversely proportional to the square root of the Reynolds number of the original shear layer. Therefore, at sufficiently high Reynolds number, the necessary condition for shear instability (Miles 1961; Howard 1961) would be fulfilled. This possibility is of interest here because secondary instability has the potential to alter the mixing efficiency of preturbulent KH billows.

With very few exceptions (Staquet 1991; Winters, MacKinnon & Mills 2003), direct numerical simulations of KH instability have been carried out at Reynolds numbers too low for secondary KH instability to develop. Evidence of secondary instability has been seen in laboratory experiments (Thorpe 1968, 1981, 1987; Atsavapranee & Gharib 1997) and in direct observations of flow in the ocean thermocline (Woods 1969). Staquet (1995) exploited the computational efficiency of two-dimensional simulations to study KH billows at higher Reynolds numbers than had been possible previously. She confirmed the validity of the Corcos–Sherman similarity theory for the braids and successfully detected the secondary instability. She also identified a new mode of instability that originates in the core regions and propagates onto the braid.

In this paper, the work of Staquet (1995) is extended to cover a broader region of parameter space. The focus is on smaller values of the initial bulk Richardson number (i.e. weakly stratified or strongly sheared flows) and on higher values of the Prandtl number. I also extend the similarity theory of Corcos & Sherman (1976) to cover cases with Prandtl number greater than unity. The lower Richardson number cases manifest secondary instability in a manner that is quite distinct from that seen in the high Richardson number flows examined by Staquet (1995). The high Prandtl number cases are needed, for example, to describe mixing of heat in water. Motivated by the superficial similarity between secondary and primary KH billows, I conduct detailed comparisons between the characteristics of secondary instability and the predictions of normal-mode stability theory applied to the braids. This comparison reveals that the secondary KH instability is actually a much more complex phenomenon than its primary counterpart. Finally, I show that the growth of secondary instability leads to a significant increase in mixing efficiency in the braid region, enhancing the importance of preturbulent billows for mixing.

The discussion begins in § 2 with a description of the mathematical model, the numerical methods used for the two-dimensional numerical simulations, and a summary and extension of the similarity theory of Corcos & Sherman (1976). In § 3, I describe results from simulations conducted over a broad region of parameter space. I test the similarity theory in detail, and investigate the effect of the initial flow parameters (i.e. Reynolds, Prandtl and bulk Richardson numbers) on the development of secondary instability. In § 4, I compute the stability characteristics of normal modes of the flow in the vicinity of the braids and compare the results with the empirically determined evolution of the secondary billows. Section 5 gives a discussion of the mixing efficiency of the preturbulent flow, focusing on the effect of secondary instability. Results are summarized in § 6.

2. Theoretical preliminaries

Early simulations of KH billows were, of necessity, conducted in two dimensions (e.g. Patnaik, Sherman & Corcos 1976; Peltier, Halle & Clark 1978). While advances in computer capacity have rendered this artifice unnecessary for some flows of interest, two-dimensional simulations are still useful for exploring high Reynolds and Prandtl number regimes. The results must be interpreted with caution, however, in the light of the known presence of three-dimensional instabilities. As KH billows grow to large amplitude, three-dimensional motions often appear first in the central regions of the cores, and later in edges of the cores and the braids. Both the stability analyses of Klaassen & Peltier (1991) and the direct numerical simulations of single KH

billows by Caulfield & Peltier (2000) showed that increasing stratification increases the dominance of core- over braid-centred three-dimensional instabilities.

Simulations of merging pairs of billows (Smyth 1999; Smyth & Moum 2000*a*) show strong three-dimensional motions developing in the cores during merging, while the braids remain substantially two-dimensional (though the results of Cortesi *et al.* (1998, 1999) suggest that the three-dimensionalization process is sensitive to the form of the initial perturbation). More recent three-dimensional simulations (K. Winters 2003, personal communication) have also shown that, under certain conditions, secondary instability can develop on the braids while the primary billows are merging, and that both the braids and the instability are purely two-dimensional during this process. These results support the validity of Staquet's (1995) two-dimensional studies of secondary instability, and have inspired the present effort to extend Staquet's results to a wider region of parameter space. The three-dimensional results also suggest caution in interpreting two-dimensional simulation results, especially flow evolution within the cores.

In this section, I will describe the methodology used for the two-dimensional simulations, as well as an extended version of the Corcos–Sherman similarity theory for the braids. The section will close with a description of the braid identification and curve-fitting methods used in comparing the simulated flows with the theory.

2.1. *The mathematical model*

The flow domain is measured by Cartesian coordinates x^* and z^* and time t^*, where asterisks indicate dimensional variables that will be non-dimensionalized below. The velocity field is assumed to be incompressible, and is therefore described by a streamfunction ψ^* and a scalar vorticity ω^*. These variables are non-dimenionalized using length scale L, velocity scale V and time scale L/V characteristic of the initial flow. Density is replaced by the non-dimensional scalar variable $\theta = -(\rho - \rho_0)/\Delta\rho$, where ρ is the fluid density, ρ_0 is a constant representative value for ρ and $\Delta\rho$ is a representative value for $|\rho - \rho_0|$. Making the Boussinesq approximation, the model equations become

$$\left.\begin{aligned} \frac{\partial\theta}{\partial t} &= -u\frac{\partial\theta}{\partial x} - w\frac{\partial\theta}{\partial z} + \frac{1}{Re_0 Pr}\nabla^2\theta, \\ \frac{\partial\omega}{\partial t} &= -u\frac{\partial\omega}{\partial x} - w\frac{\partial\omega}{\partial z} + Ri_0\frac{\partial\theta}{\partial x} + \frac{1}{Re_0}\nabla^2\omega, \\ u &= -\frac{\partial\psi}{\partial z}, \quad w = \frac{\partial\psi}{\partial x}, \quad \nabla^2\psi = \omega. \end{aligned}\right\} \tag{2.1}$$

These equations contain three non-dimensional parameters: the Reynolds number $Re_0 = VL/\nu$, the bulk Richardson number $Ri_0 = g\Delta\rho L/\rho_0 V^2$ and the Prandtl number $Pr = \nu/\kappa$. The constants g, ν and κ represent gravitational acceleration, viscosity and mass diffusivity, respectively. The subscripts on Re_0 and Ri_0 indicate that these are initial values of parameters that change as the flow evolves.

2.2. *Two-dimensional simulations*

Simulations of two-dimensional KH billows are carried out in a horizontally periodic domain with periodicity interval $-L_x/2 < x < L_x/2$ and vertical extent $-L_z/2 < z < L_z/2$. The periodicity interval is $L_x = 27.9$, twice the wavelength of the fastest-growing primary instability (e.g. Hazel 1972). The slight Ri_0 dependence of this wavelength is neglected. The domain height is set to $L_z = 0.75L_x$, sufficient to minimize the influence of the upper and lower boundaries, where zero-flux conditions ($\partial\theta/\partial z = \omega = 0$) apply.

Sequence	Run #	Re_0	Pr	Ri_0	Grid size
Resolution	1	1000	1	0.08	512×768
	2	1000	1	0.08	256×385
	3	1000	1	0.08	192×289
	4	1000	1	0.08	128×193
	5	1000	1	0.08	96×145
Reynolds number	1	1000	1	0.08	512×768
	6	2000	1	0.08	512×768
	7	4000	1	0.08	512×768
	8	6000	1	0.08	768×1153
Prandtl number	6	2000	1	0.08	512×768
	9	2000	2	0.08	512×768
	10	2000	3	0.08	768×1153
	11	2000	5	0.08	1024×1537
	12	2000	7	0.08	1024×1537
Richardson number	13	2000	1	0.04	512×768
	14	2000	1	0.06	512×768
	6	2000	1	0.08	512×768
	15	2000	1	0.10	512×768
	16	2000	1	0.12	512×768
	17	2000	1	0.14	512×768
	18	2000	1	0.16	512×768

TABLE 1. Parameter values for the various sequences of two-dimensional simulations.

Simulations are initialized with a parallel flow in which shear and stratification are concentrated in a horizontal layer surrounding the plane $z = 0$:

$$\omega(x, z, 0) = -\mathrm{sech}^2 z, \tag{2.2}$$

$$\theta(x, z, 0) = \tanh z. \tag{2.3}$$

Added to this initial state is a vorticity perturbation designed to stimulate primary and pairing instabilities:

$$\omega_{pert} = a\,\mathrm{sech}^2 z \left\{ \left(k_o^2 + 2(1 - 3\tanh^2 z)\right) \cos(k_o x) - b\left(k_o^2/4 + 2(1 - 3\tanh^2 z)\right) \cos\left(\tfrac{1}{2}k_o x\right) \right\} \tag{2.4}$$

where k_o is the non-dimensional wavenumber of the fast-growing mode and a and b are constants having the values 0.01 and 0.8, respectively. Because the initial perturbation is weak enough to obey linear physics (i.e. $a \ll 1$), its precise form has little effect on the quantities of interest here. (See Staquet (1995) for a detailed discussion of the effects of significant variations in the initial perturbation.)

Computations are performed on a rectangular mesh $x_i; i = 1, 2, \ldots, N_x,\ z_k;\ k = 1, 2, \ldots, N_z$. Spatial discretization is Fourier pseudospectral in the horizontal and fourth-order compact (Lele 1992) in the vertical. Because the pseudospectral scheme used in the horizontal is intrinsically more accurate than the compact method used in the vertical, the vertical grid spacing Δz is chosen to be one half the horizontal spacing Δx. (Detailed tests of spatial resolution are described in § 3.) Time stepping is accomplished using a third-order Adams–Bashforth method.

A dataset of eighteen simulations forms the basis for the present analyses. Sequences of simulations were designed to examine the effects of variations in spatial resolution, initial Reynolds number, Prantdl number and initial bulk Richardson number (table 1).

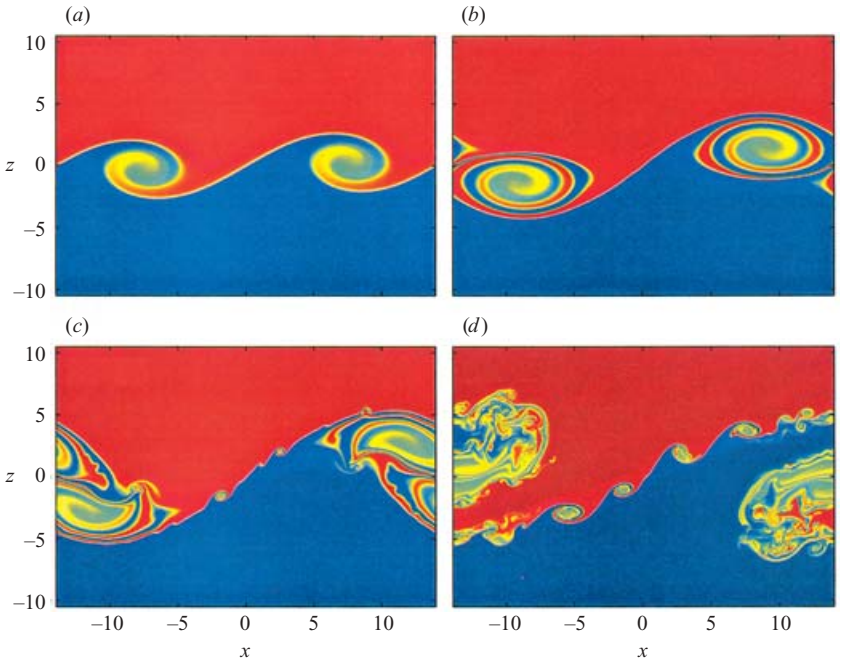

FIGURE 1. Evolution of the scalar field $\theta(x, z, t)$ for simulation #8. Colour indicates values ranging from -1 (blue) to $+1$ (red).

Figure 1 shows a sample result. At $t = 39$ (figure 1*a*), the primary KH wavetrain has reached maximum amplitude. The computational domain contains two billows and two braids. By $t = 60$, pairing has begun. One braid has vanished. At the centre of the remaining braid ($x = z = 0$) is a stagnation point, the nexus of much of the physics to be discussed here. Pairing is well underway at $t = 69$, and secondary instability is visible on the braid. By $t = 81$, pairing is almost complete. Secondary billows have reached large amplitude by this time and have, in some instances, paired.

2.3. *Equilibrium similarity theory*

I now describe the Corcos–Sherman similarity theory for the braid regions. This development differs from Corcos & Sherman (1976) in that I focus only on steady-state solutions and I extend the results to $Pr > 1$. I begin by rewriting the equations of motion in a coordinate frame tilted at an angle ϕ counterclockwise from the horizontal:

$$\left.\begin{aligned} \frac{\partial\theta}{\partial t} &= -u'\frac{\partial\theta}{\partial x'} - w'\frac{\partial\theta}{\partial z'} + \frac{1}{Re_0 Pr}\nabla'^2\theta, \\ \frac{\partial\omega}{\partial t} &= -u'\frac{\partial\omega}{\partial x'} - w'\frac{\partial\omega}{\partial z'} + Ri_0\left(\cos\varphi\frac{\partial\theta}{\partial x'} - \sin\varphi\frac{\partial\theta}{\partial z'}\right) + \frac{1}{Re_0}\nabla'^2\omega, \\ u' &= -\frac{\partial\psi'}{\partial z'}, \quad w' = \frac{\partial\psi'}{\partial x'}, \quad \nabla'^2\psi' = \omega. \end{aligned}\right\} \tag{2.5}$$

Primes indicate coordinate-dependent quantities evaluated in the tilted coordinate system. The intention is that φ will be chosen so that the x'-axis is locally parallel to the braid.

I now make three simplifying assumptions. I first assume that, for suitably chosen φ, gradients in the z'-direction are much greater than those in x', so that the latter may be neglected. The sole exception to this is the streamfunction, whose x' derivative, w', is retained and assumed to have the form $w' = -\gamma z'$. The constant γ quantifies a uniform strain field, oriented so that z' is the direction of maximum compression. Finally, I assume that the braid region is close to equilibrium, so that time derivatives can be neglected.

The result of these assumptions is a pair of ordinary differential equations for the scalar and vorticity fields in the vicinity of the braid:

$$0 = \gamma z' \frac{\mathrm{d}\theta}{\mathrm{d}z'} + \frac{1}{Re_0 Pr} \frac{\mathrm{d}^2\theta}{\mathrm{d}z'^2}, \tag{2.6}$$

$$0 = \gamma z' \frac{\mathrm{d}\omega}{\mathrm{d}z'} - Ri_0 \sin\varphi \frac{\mathrm{d}\theta}{\mathrm{d}z'} + \frac{1}{Re_0} \frac{\mathrm{d}^2\omega}{\mathrm{d}z'^2}. \tag{2.7}$$

These equations describe a state in which the scalar profile $\theta(z')$ is in equilibrium due to a balance between compressive strain and diffusion, and the vorticity profile $\omega(z')$ is in equilibrium due to a balance among compressive strain, baroclinic torque and viscosity. It will be seen that the braid approaches this equilibrium state late in the pairing process.

The scalar equation (2.6) is easily solved to obtain

$$\theta = \frac{\Delta\theta}{2} \operatorname{erf}\left(\frac{\pi^{1/2}}{2} \frac{z'}{\delta_\theta}\right) \tag{2.8}$$

in which $\Delta\theta$ and δ_θ are constants. The scalar thickness δ_θ is given by

$$\delta_\theta = \left(\frac{\pi}{2\gamma Re_0 Pr}\right)^{1/2}. \tag{2.9}$$

$\Delta\theta$, the net change in θ across the braid, is not determined. In practice, we will see that its value is usually slightly less than 2, i.e. the scalar differential across the braid contains nearly the entire scalar change across the domain. The maximum scalar gradient occurs at $z' = 0$ and is given by

$$\theta^o_{z'} = \frac{\Delta\theta}{2\delta_\theta}. \tag{2.10}$$

Solution of the vorticity equation is less straightforward. I begin by defining the similarity variables η and H:

$$\eta = \frac{z'}{\delta_\theta}, \quad H(\eta) = \frac{\gamma Pr \delta_\theta}{2Ri_0 \sin\varphi \Delta\theta} \omega(z'). \tag{2.11}$$

In terms of these variables, the vorticity equation reduces to

$$\frac{\mathrm{d}^2 H}{\mathrm{d}\eta^2} + \frac{2\eta}{Pr} \frac{\mathrm{d}H}{\mathrm{d}\eta} = \mathrm{e}^{-\eta^2}. \tag{2.12}$$

For the special case $Pr = 1$, (2.12) has the solution

$$H = -\tfrac{1}{2}\mathrm{e}^{-\eta^2}. \tag{2.13}$$

When $Pr \neq 1$, (2.12) is most readily solved numerically. As shown in figure 2, the numerical solution is fitted well by the more general Gaussian function

$$H = H_0 \mathrm{e}^{-(\eta/R)^2} \tag{2.14}$$

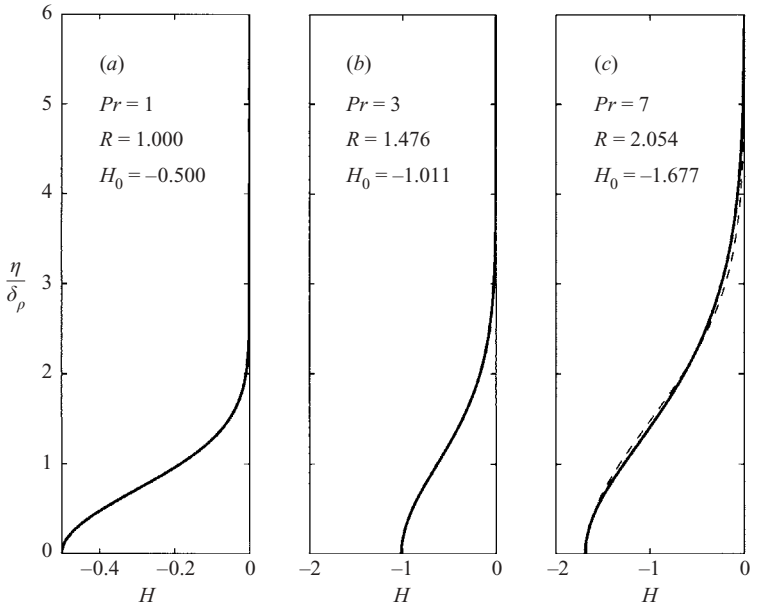

FIGURE 2. Numerical solutions of (2.12) for representative values of the Prandtl number. Because solutions are even, only the half-domain $\eta > 0$ is shown. Boundary conditions are $\mathrm{d}H/\mathrm{d}\eta = 0$ at $\eta = 0$ and $H \to 0$ as $|\eta| \to \infty$. Fitted values of H_0 and R are indicated.

where $H_0(Pr) = H|_{\eta=0}$ and $R(Pr)$ is the ratio of the vorticity thickness to the scalar thickness of the braid. The fit was performed using the Nelder–Mead simplex method (Press *et al.* 1992) to minimize the squared error.

For most of the work described here, I focus on the range $1 \leqslant Pr \leqslant 7$. In that range, the dependence of the parameters R and H_0 upon Pr is fitted well by the power laws

$$R = Pr^{\alpha}, \qquad H_0 = -\tfrac{1}{2} Pr^{\beta}, \tag{2.15}$$

with $\alpha = 0.3635$ and $\beta = 0.6307$ (figure 3).

To summarize, the approximate solution of (2.7) for $1 \leqslant Pr \leqslant 7$ is

$$\omega(z') = \omega^{o} \exp[-(z'/\delta_{\omega})^2], \tag{2.16}$$

in which the maximum vorticity is

$$\omega^{o} = -\left(\frac{2}{\pi}\right)^{1/2} \frac{{Re_0}^{1/2}\, Ri_0 \sin\varphi \Delta\theta\, Pr^{\beta-1/2}}{\gamma^{1/2}}, \tag{2.17}$$

and the vorticity thickness is

$$\delta_{\omega} \equiv R\delta_{\theta} = \left(\frac{\pi}{2\gamma Re_0}\right)^{1/2} \frac{1}{Pr^{1/2-\alpha}}. \tag{2.18}$$

Note that, in the absence of buoyancy effects, δ_{ω} would be independent of the Prandtl number, i.e. α would equal one half. Thus, the non-zero value of $1/2 - \alpha$ is a measure of the effect of buoyancy forcing on the vorticity thickness of the braid. We may also integrate (2.16) to obtain a theoretical profile for the braid-parallel velocity:

$$u' = \frac{\Delta u}{2} \operatorname{erf}\left(\frac{\pi^{1/2}}{2} \frac{z'}{\delta_{\omega}}\right), \tag{2.19}$$

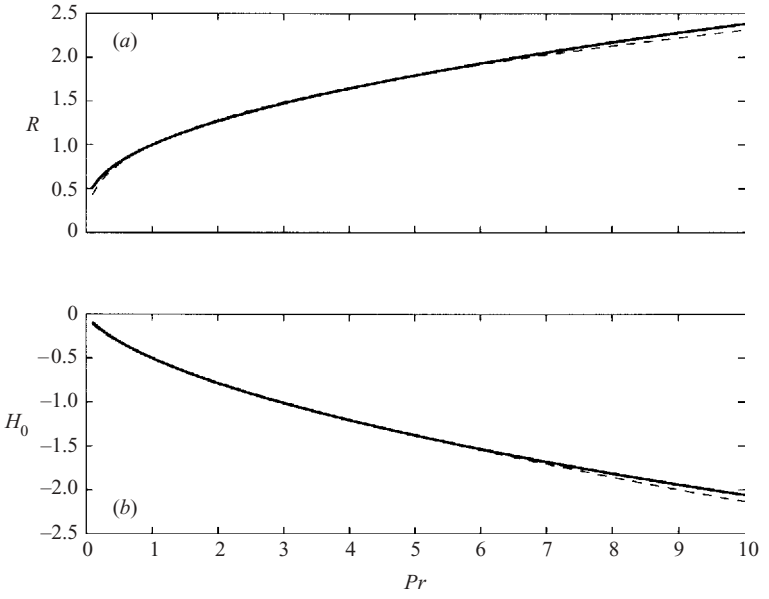

FIGURE 3. $R(Pr)$ and $H(Pr)$, obtained as shown in figure 2. Dashed curve: fit to (2.15) with $\alpha = 0.3635$ and $\beta = 0.6307$. These values are optimized for the range $1 \leqslant Pr \leqslant 7$.

in which the velocity change across the braid is

$$\Delta u = 2\delta_\omega \omega^o = -\frac{\pi^{1/2} Ri_0 \sin\varphi \Delta\theta Pr^{\alpha+\beta-1}}{\gamma}. \tag{2.20}$$

In the following section, these predicted profile shapes will be compared with profiles obtained from numerical simulations in order to validate the equilibrium similarity theory.

The similarity theory also allows us to make *a priori* predictions about the dependence of secondary instability upon the initial conditions as represented by the parameters Re_0, Pr and Ri_0. These predictions will be tested in § 3, and will be extended using explicit linear stability analyses in § 4. Unstable modes of a stratified shear layer with similar shear and density scales grow exponentially with rate $\sigma = Sf(Ri)$, where S is the maximum shear and f is a non-dimensional, decreasing function of the bulk Richardson number, Ri, that drops to zero for $Ri > 1/4$ (e.g. Hazel 1972). In the present case, the maximum shear is found at the centre of the braid and is given by ω^o (cf. (2.17)), while the bulk Richardson number that characterizes the stability of the braid is

$$Ri' = \frac{Ri_0 \cos\varphi \theta^o_{z'}}{\omega^{o\,2}} = \frac{(2\pi)^{1/2} \gamma^{3/2} Pr^{3/2-\beta}}{Re_0^{1/2} Ri_0 \Delta\theta \sin\varphi \tan\varphi}. \tag{2.21}$$

The central vorticity and Richardson number of the braid are functions of six parameters: the strain γ, the tilt angle φ, the scalar differential $\Delta\theta$, and the Reynolds, Prandtl and Richardson numbers. The first two variables, γ and φ, represent the large-scale structure of the primary KH instability; they depend somewhat on Ri_0, but very little on Re_0 or Pr. The scalar differential $\Delta\theta$ is usually slightly less than 2.0.

Since increasing Re_0 both increases ω^o and decreases Ri', we can predict with confidence that increasing Re_0 promotes secondary instability (as did Corcos & Sherman 1976). The effect of increasing Pr is ambiguous, since it increases ω^o but

also increases Ri'. The inverse proportionality of Ri' to Ri_0 reflects the fact that the shear in the braid is driven by buoyancy effects. In the singular limit $Ri_0 \to 0$, this mechanism for braid reinforcement is absent, and secondary instability occurs rarely if ever (e.g. Dritschel *et al.* 1991). Increasing Ri_0 leads to both increasing ω^o and decreasing Ri', suggesting enhanced likelihood of secondary instability. We will see, however, that this effect is complicated by the strong dependence of φ on Ri_0.

2.4. *Fitting procedures*

In order to test the theoretical predictions of the previous subsection, we must have methods for computing the relevant parameters from numerically simulated flow fields. In this subsection, I describe those methods and give detailed examples of their use at two times during a representative simulation. In the next section, the computed parameters will be presented as continuous functions of time over the duration of each simulation. The objectives are to identify a central portion of the braid in a given set of computed flow fields, average along the braid to obtain profiles of $\theta(z')$ and $u'(z')$, and fit the results to appropriate functions in order to obtain values of the braid parameters δ_θ, δ_ω, $\Delta\theta$ and ω^o. When the primary KH billows are well into the pairing phase (e.g. figure 1*b*), the fits are very close, and the details of the procedures used to obtain the fits are of little consequence. At other times, however, the braid can be far from its equilibrium state, and the fits must be done with care for the results to be physically meaningful.

I begin by identifying a central portion of the braid. For each x in the range $-L_x/8 < x < L_x/8$, I scan over z to find the height $z_b(x)$ at which the scalar gradient magnitude $|\nabla\theta|$ is maximized. (First, the maximum value on the computational grid is found, then it and the values at the two neighbouring grid points are fitted to a parabola, the maximum of which furnishes the final value of z_b.) Near equilibrium, $z_b(x)$ is almost linear, but at other times the function exhibits significant curvature. Therefore, taking account of the symmetry of the flow, I fit $z_b(x)$ to a cubic polynomial of the form

$$z_f(x) = a_f x + b_f x^3. \tag{2.22}$$

With appropriate values for the coefficients, this function coincides almost exactly with the maximum scalar gradient except when the braid is distorted by secondary instability. In the latter situation, $z_f(x)$ provides a useful indication of the undisturbed position of the braid, and thus a basis for measuring the amplitude of the instability. The tilt angle φ is identified as the local slope of $z_f(x)$, i.e. $\tan\varphi = \mathrm{d}z_f/\mathrm{d}x$ (figure 4).

I next repeat the scan over the reduced range $-L_x/16 < x < L_x/16$, this time identifying, at each x_i, a line segment locally perpendicular to $z_f(x_i)$ and having length $\cos(\varphi)L_z/4$. Along each line segment, a grid of points $z'_j = j\,\Delta z$ is defined, where Δz is the vertical spacing of the computational grid and z' is the distance along the line segment measured from its centre at x_i, $z_f(x_i)$. At each such point, values of $u'_i(z')$, $w'_i(z')$ and $\theta_i(z')$ are computed via bilinear interpolation from the computational grid and recorded. I complete this phase of the calculation by averaging over the index i to obtain profiles $u'(z')$, $w'(z')$ and $\theta(z')$, along with an averaged value of φ.

The next step is to fit these profiles to functions appropriate for comparison with the equilibrium similarity scaling described above. Both $\theta(z')$ and $u'(z')$ are fitted to a function of the form

$$F(z') = v_1 v_2 \operatorname{erf}\left(\sqrt{\frac{\pi}{4}}\frac{z' - v_5}{v_2}\right) + v_3 z' + v_4. \tag{2.23}$$

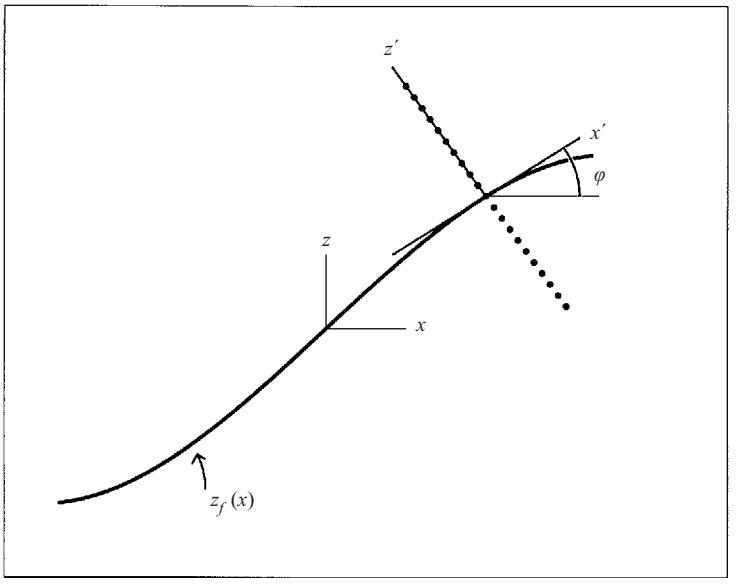

FIGURE 4. Schematic of braid coordinates. The thick curve represents a small segment near the centre of the braid. The curvature of the braid segment is exaggerated. Dots represent the line of points at which flow quantities are computed for a given i.

This function is a generalization of the equilibrium similarity solutions (2.8) and (2.19). The thickness (scalar or vorticity, as the case may be) is given by v_2. The gradient at the centre of the braid is $v_1 + v_3$, and the net change across the braid is $2v_1v_2$. The constants v_3, v_4 and v_5 are zero in (2.8) and (2.19). The fitted values of these constants are also very nearly zero when the braid is close to equilibrium; they are included in (2.23) so as to improve the fit, and thus to provide a meaningful description of the braid, at earlier times in the flow evolution. These fits required solution of a nonlinear optimization problem, and were performed using the Nelder–Mead simplex method (Press *et al.* 1992).

The braid-perpendicular velocity $w'(z')$ is fitted to the general cubic polynomial

$$P(z') = p_1 + p_2 z' + p_3 z'^2 + p_4 z'^3. \tag{2.24}$$

The strain rate γ is identified with minus the derivative of w' at $z' = 0$, i.e. $\gamma = -p_2$. The remaining coefficients p_1, p_3 and p_4 are close to zero when the braid is near equilibrium.

I close this section with an example of the analyses described above applied at two separate times in a sample simulation with $Re_0 = 1000$, $Ri_0 = 0.08$ and $Pr = 1$. Figure 5 contains flow visualizations for this case. Figure 6 shows cross-profiles of scalar and velocity, and table 2 shows the results of fitting the computed profiles to the forms (2.23) and (2.24) described above at times $t = 27$ (figure 5*a*) and $t = 72$ (figure 5*b*).

At $t = 27$, primary KH billows have attained large amplitude but have not yet begun to pair (figure 5*a*). The profiles differ significantly from the theoretical equilibrium forms. Both the θ- and the u'-profiles show strong gradients away from the braid, and w' exhibits strong curvature. Nevertheless, the fitted parameter values furnish useful measures of scalar thickness ($\delta_\theta = v_{\theta 2} = 0.038$), vorticity thickness ($\delta_\omega = v_{u2} = 0.699$), net scalar differential across the braid ($\Delta\theta = 2v_{\theta 1}v_{\theta 2} = 1.42$) and maximum vorticity ($\omega^o = v_{u1} = 0.844$). The strain at the centre of the braid is $\gamma = -p_2 = 0.134$.

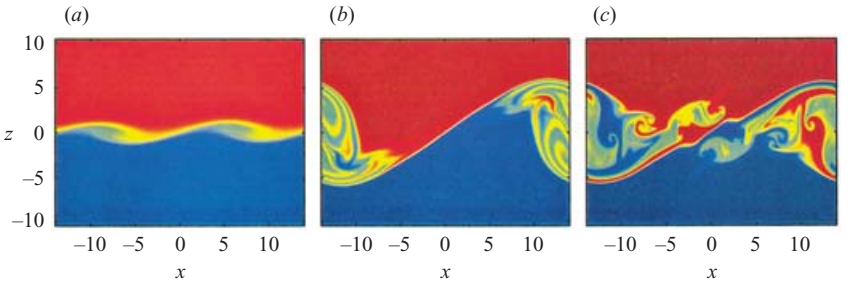

FIGURE 5. Merging KH billows in run #1, with $Re_0 = 1000$, $Ri_0 = 0.08$, $Pr = 1$. Colour indicates the scalar field θ, with values ranging from -1 (blue) to $+1$ (red). In (b), the braid is close to the predicted equilibrium state. Indications of secondary instability appeared just before the braid was engulfed by the collapsing core (c).

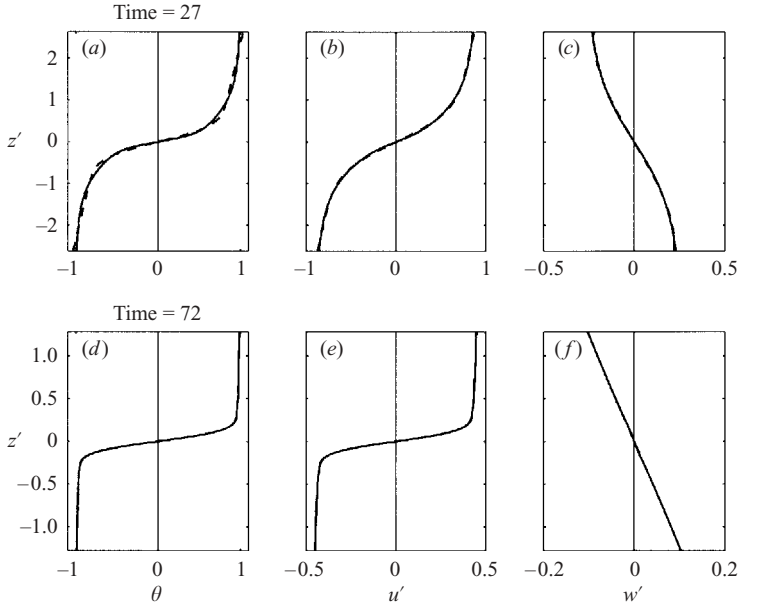

FIGURE 6. Profiles of the scalar θ (a, d), the braid-parallel velocity u' (b, e) and the braid-perpendicular velocity w' (c, f) as functions of the braid-perpendicular coordinate z'. Results are shown at $t = 27$ (a, b, c) and $t = 72$ (d, e, f). Dashed curves indicate fitted functions as described in § 2.4.

$t = 27$					
v_θ	1.877	0.380	0.123	0.000	−0.004
v_u	0.844	0.699	0.109	0.000	−0.004
p	−0.001	−0.134	0.000	0.007	
$t = 72$					
v_θ	7.433	0.128	0.032	0.000	0.000
v_u	3.226	0.130	0.024	−0.001	0.000
p	0.000	−0.082	0.000	0.001	

TABLE 2. Fitted values of the braid parameters for the flows shown in figure 5 and 6, computed as described in § 2.4.

At $t = 72$, pairing is well underway (figure 5*b*). The profile shapes closely resemble the theoretical equilibrium forms, as may be seen by the reduced values of $v_{\theta 3}$, $v_{\theta 5}$, v_{u3}, v_{u5} and p_4. The scalar thickness and the vorticity thickness are now nearly equal, as we expect when $Pr = 1$ ($\delta_\theta = 0.128$, $\delta_\omega = 0.130$). The net scalar differential across the braid is $\Delta\theta = 1.90$, close to the maximum possible value 2.0. The shear at the braid centre has increased to $\omega^o = 3.23$, a four-fold increase over the value at $t = 27$, while the strain has decreased to 0.082.

3. Braid evolution

In this section, I describe the evolution of the braids in numerical solutions of the initial value problem described in §§ 2.1 and 2.2. The objectives are (i) to examine the structure of the braid during the pairing of the primary billows and compare with the predictions of equilibrium similarity theory developed in § 2.3, and (ii) to investigate the evolution of secondary instability on the braids as a function of the Reynolds, Prandtl and Richardson numbers. The discussion begins in § 3.1 with introductory discussions of the braid structure and the effects of spatial resolution in a relatively simple example. I then describe the results of sequences of simulations in which Re_0, Pr and Ri_0 were varied in turn (§§ 3.2, 3.3 and 3.4).

3.1. *Primary instability, braid structure and spatial resolution*

This preliminary discussion surveys results from run #1 (see figure 5). This was a case with relatively low Reynolds number ($Re_0 = 1000$), and was typical except in that it did not develop secondary instability except possibly at the very end of the merging process (figure 5*c*). Complications due to secondary instability will be introduced later.

Both the tilt angle (figure 7*a*) and the strain rate (figure 7*b*) increased initially to maximum values then decreased. The strain reached its maximum of 0.18 around the time that the primary KH instability attained maximum amplitude and began to pair. The angle continued to increase through the early part of the pairing process, reaching a maximum of 40° near $t = 63$. As the paired billows rotated past the point of maximum vertical extent, the tilt angle decreased rapidly, then levelled off at a value just under 30°. During the same time, the strain decreased rapidly to a value of 0.08. This approximate halving of the strain corresponds to the doubling of the primary vortex spacing during pairing (e.g. Staquet 1995).

Both measures of the braid thickness (figures 7*c* and 7*d*) decreased by an order of magnitude during the early growth of the primary instability, then stabilized at values very close to those predicted by equilibrium similarity theory. The scalar differential $\Delta\theta$ stabilized at a value just below 2.0, indicating that the braid encompassed almost the entire scalar change across the computational domain. (The velocity change across the braid, not shown here, was only about 1/3 of the net change across the domain.) The shear at the centre of the braid increased by a factor of 3 during pairing. Correspondence with the prediction of equilibrium stability theory was not as close as in the case of the length scales (figure 7*c*, *d*), but was quite good during the two intervals $40 < t < 50$ and $75 < t < 85$, when the strain rate and the tilt angle (figure 7*a*, *b*) evolved least rapidly. I conclude that, for this simulation at least, equilibrium similarity theory adequately describes the braid shear when the properties of the primary instability that govern the braid are slowly varying (i.e. when the assumptions underlying the theory are satisfied).

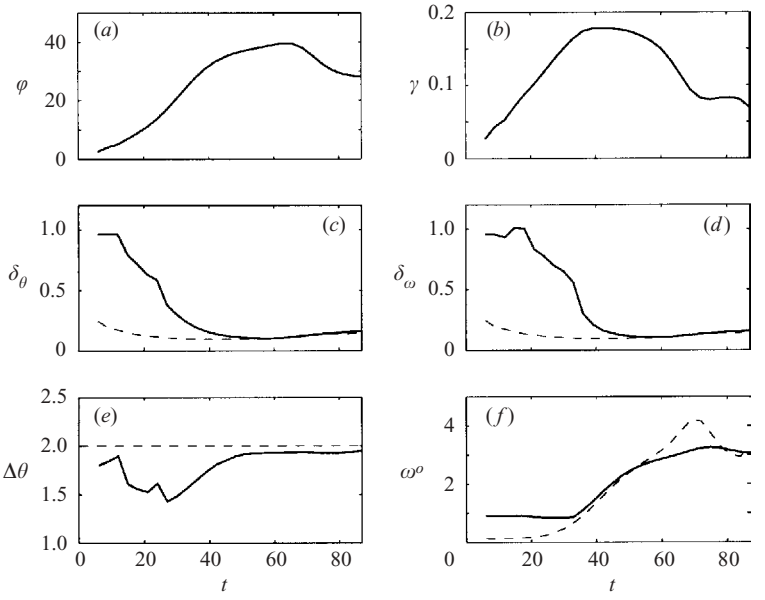

FIGURE 7. Histories of the tilt angle (*a*), the strain rate (*b*), the scalar thickness (*c*), the vorticity thickness (*d*), the scalar differential across the braid (*e*) and the vorticity at the braid centre (*f*), for run #1. Solid curves are quantities computed from simulation results using the methods of §2.4. Dashed curves are reference values of the corresponding quantities. The reference thicknesses and central vorticity are predicted via equilibrium similarity theory (2.9), (2.18), (2.17). The reference value of the scalar differential $\Delta\theta$ is just the net change across the domain, 2.0. All quantities are non-dimensional.

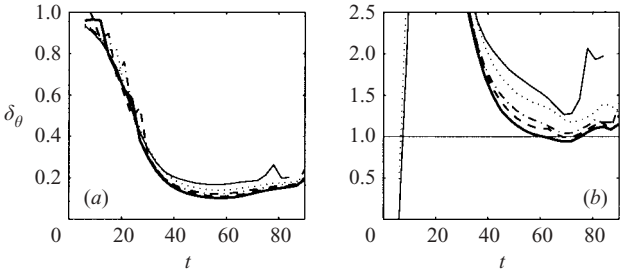

FIGURE 8. Histories of (*a*) the scalar thickness, and (*b*) the thickness scaled by the theoretical value computed using (2.9). Curve types indicate different array sizes: thick solid curve: run #1 (512×768); dashed curve: run #2 (256×385); dash-dotted curve: run #3 (192×289); dotted curve: run #4 (128×193); thin solid curve: run #5 (96×145). For all cases, $Re_0 = 1000$, $Ri_0 = 0.08$ and $Pr = 1$.

The accuracy of these simulations depends heavily on spatial resolution. Figure 8(*a*) shows the evolution of the scalar thickness in a sequence of simulations similar to run #1 except that the spatial resolution was varied. Reduced resolution is seen to result in an unrealistically thick braid. Figure 8(*b*) shows the scalar thickness normalized at each point in time by the value predicted by equilibrium similarity theory. In the two simulations represented by the thick solid curve and the dashed curve (the most finely resolved cases), the braid thicknesses matched both each other and the theoretical value to within a few percent during the period $55 < t < 75$. In all other

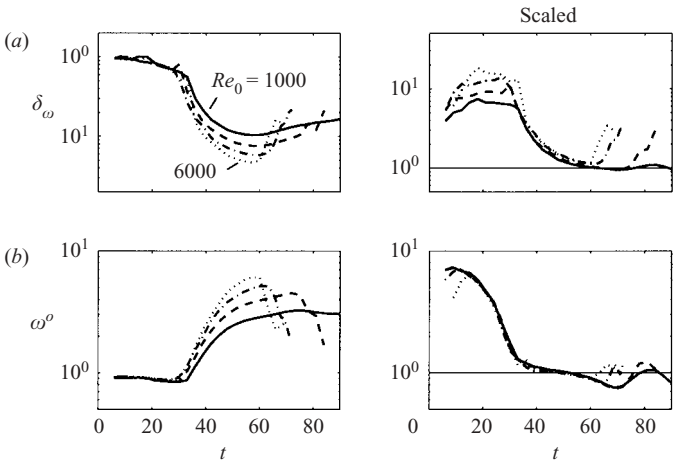

FIGURE 9. Histories of (*a*) the scalar thickness, (*b*) the braid vorticity. Right-hand frames show the same quantities scaled using (2.9) and (2.17). Curve types indicate initial Reynolds number: thick solid curve: run #1 ($Re_0 = 1000$); dashed curve: run #6 ($Re_0 = 2000$); dash-dotted curve: run #7 ($Re_0 = 4000$); dotted curve: run #8 ($Re_0 = 6000$). In all cases, $Ri_0 = 0.08$, $Pr = 1$. Curves are terminated shortly after the appearance of secondary instability.

cases, resolution was coarser than this, and both convergence and agreement with the theoretical scaling were significantly degraded. I regard the second case as marginally resolved for the present purposes. In all of the simulations discussed below, the resolution of the braid was intermediate between those of the first and second cases shown in figure 8.

3.2. *Dependence on the initial Reynolds number*

Figure 9 shows representative properties of the braid during a sequence of four simulations in which the Reynolds number was varied between 1000 (solid curve) and 6000 (dotted curve). The tilt angle and strain rate histories vary little with Re_0, and are thus nearly identical to those shown in figure 7(*a*, *b*). Both the minimum vorticity thickness and the maximum vorticity varied by factors of 2.5 over this range of Re_0. In the $Re_0 = 6000$ case, the braid thickness reached a minimum of 0.045 times the initial shear layer thickness, while the maximum braid shear was over six times that of the original shear layer. The Reynolds number dependence of the braid thickness is collapsed to within 10% by the theoretical scaling. The braid shear is not described as accurately: the simulated braid shears tended to drop below the equilibrium value after about $t = 60$. Nevertheless, the variability due to Reynolds number is reduced from a factor of 2.5 to a few tens of percent by the equilibrium scaling.

In the $Re_0 = 6000$ case, beginning around $t = 60$, both the braid thickness and the shear departed rapidly from the equilibrium scaling. This is the signature of secondary instability. The same behaviour is evident at later times in the $Re_0 = 4000$ and $Re_0 = 2000$ cases. The $Re_0 = 1000$ case shows no evidence of secondary instability. Figure 10 shows the θ-field for the $Re_0 = 4000$ case after the secondary billows had grown to large amplitude. Billows occur in three distinct groups. At the stagnation point (near the centre of the image), a pair of small billows is just emerging. The large billows to the left and right of the stagnation point emerged in similar fashion originally, and have now grown while being advected outward by the extensional strain. Further to the right is a periodic train of three billows, followed by a smaller

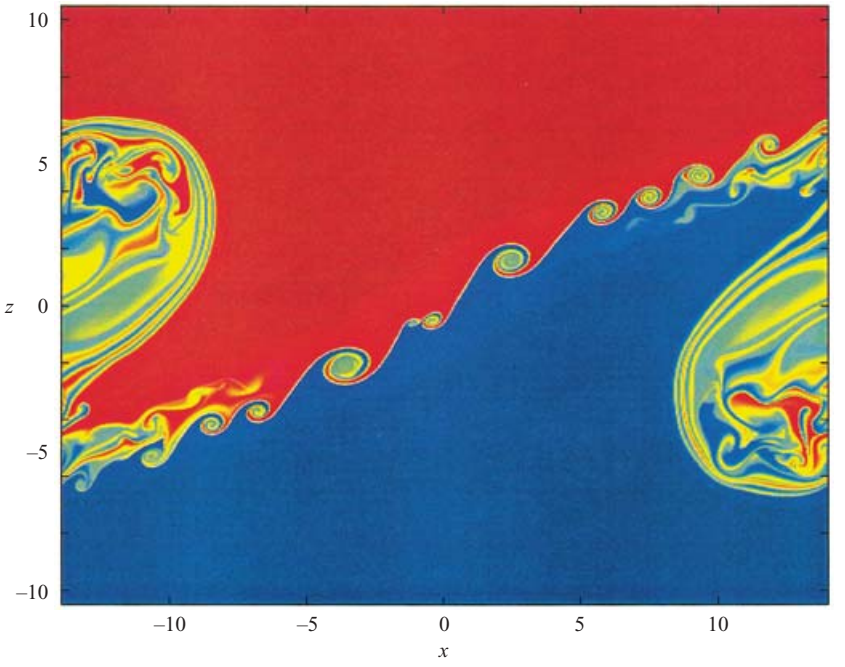

FIGURE 10. Scalar field $\theta(x, z, t)$ for simulation #7 at $t = 78$, showing secondary billows. Values range from -1 (blue) to $+1$ (red).

fourth billow. This group first appeared just to the left of the position shown and is propagating to the right . Below and to the right of each of these billows is a weaker vortex of opposite sign, suggesting the sinuous instability of a jet originating at the edge of the core. This indicates the influence of the 'near-core' instability discovered by Staquet (1995). A corresponding, though somewhat weaker, train of secondary billows is visible at the left-hand end of the braid.

3.3. *Dependence on the Prandtl number*

Braid properties for a sequence of cases with Prandtl numbers ranging from 1 to 7 are shown in figure 11. The tilt angle and strain rate are not shown, as they are insensitive to Pr and evolve nearly as shown in figure 7(a, b). The scalar thickness δ_θ of the braid varies strongly as a function of Prandtl number (figure 11a). The equilibrium scaling (2.9) collapses this variability very effectively when the braid is near equilibrium (figure 11b, $t \sim 40$–60). Also well described by the theoretical scaling are the weaker dependence of the vorticity thickness on Pr (figure 11c, d), and that of the scale ratio (figure 11e, f), in the interval $40 < t < 60$. Fits are poor at earlier times because the braid has not yet attained its equilibrium state, and at later times because the equilibrium is upset by secondary instability.

Rapid departures of the layer thicknesses from equilibrium scaling (figure 11b, d, $t > 60$) happen first in the higher Prantdl number cases. Therefore, although attempts to predict the dependence of secondary instability on Prandtl number based on equilibrium similarity theory were inconclusive (§ 2.3), it is clear that instability appeared first at high Prandtl numbers. Figure 12 shows the evolution of several quantities related to the stability of the braid as computed from the simulations. As predicted by the theory, the braid shear increased slightly with increasing Prandtl number (figure 12a); however, the stabilizing scalar gradient across the braid increased

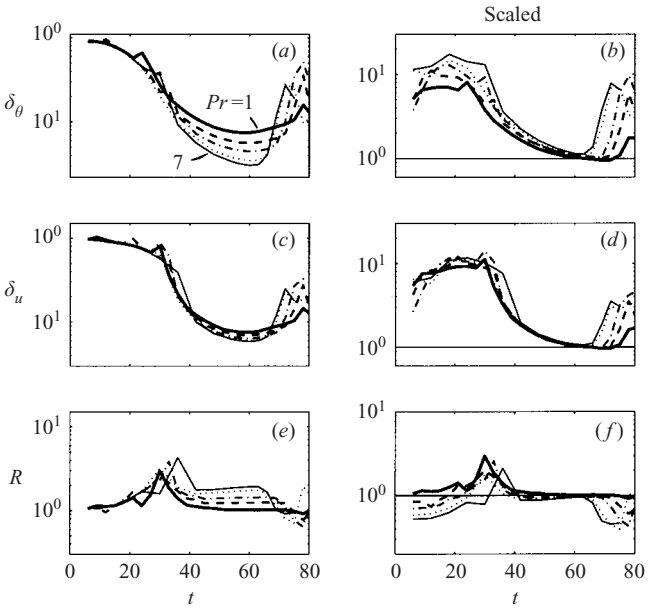

FIGURE 11. Histories of (a, b) the scalar thickness, (c, d) the vorticity thickness and (e, f) the scale ratio. Right-hand frames show the same quantities scaled using (2.9), (2.17) and (2.15). Curve types indicate Prandtl number: thick solid curve: run #6 ($Pr=1$); dashed curve: run #9 ($Pr=2$); dash-dotted curve: run #10 ($Pr=3$); dotted curve: run #11 ($Pr=5$); thin solid curve: run #12 ($Pr=7$). In all cases, $Ri_0=0.08$, $Re_0=2000$.

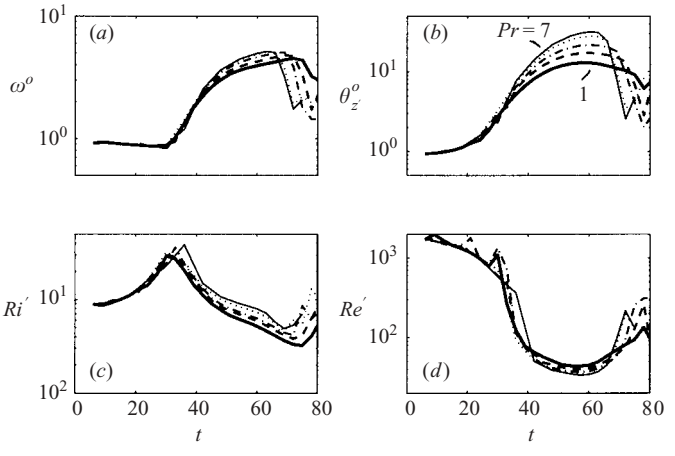

FIGURE 12. Histories of (a) the shear and (b) the scalar gradient at the braid centre, (c) the braid Richardson number and (d) the braid Reynolds number. Curve types indicate Prandtl number: thick solid curve: run #6 ($Pr=1$); dashed curve: run #9 ($Pr=2$); dash-dotted curve: run #10 ($Pr=3$); dotted curve: run #11 ($Pr=5$); thin solid curve: run #12 ($Pr=7$). In all cases, $Ri_0=0.08$, $Re_0=2000$.

much more dramatically (figure 12*b*). The braid Richardson number, which quantifies the competition between these two effects, increased with increasing Pr as predicted by the theory. In addition, the braid Reynolds number $Re'=\delta_\omega^2\omega^o/\nu$ decreased with increasing Pr. These latter two results suggest that increasing Pr should stabilize the

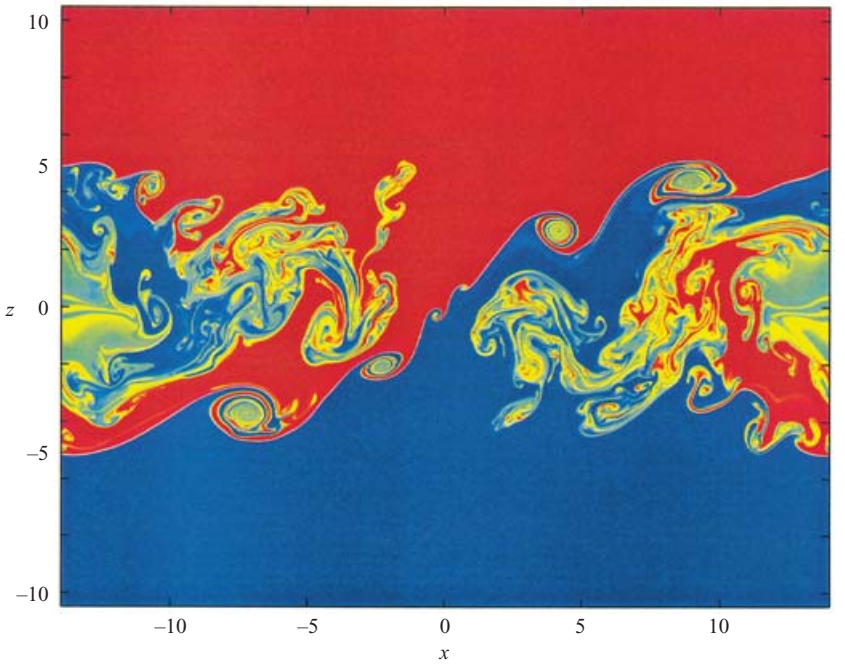

FIGURE 13. Scalar field $\theta(x, z, t)$ for simulation #12 at $t = 90$, showing secondary billows. Values range from -1 (blue) to $+1$ (red).

braid. Apparently, though, the slight increase of ω^o with Pr dominates and causes higher values of Pr to favour secondary instability.

Figure 13 shows the $Pr = 7$ case at an advanced stage, just as the braid was about to be engulfed by the cores. Three pairs of secondary billows are visible. Each pair appeared originally at the stagnation point and was subsequently advected away as it grew. Periodic trains of billows like those seen in the $Re_0 = 4000$, $Pr = 1$ case (figure 10) appeared briefly but had been advected into the cores by the time shown here. Note that the small-scale details of the flow within the core region are likely to be inaccurate at this late time due to the suppression of three-dimensional instabilities. Even the largest of the secondary billows might manifest three-dimensional features by this late stage, if the model allowed it.

3.4. *Dependence on the initial bulk Richardson number*

Unlike Re_0 and Pr, the initial bulk Richardson number, Ri_0, is a dominant factor governing the evolution of the primary KH instability. Figures 14(*a*) and 14(*b*) show tilt angle and strain rate histories from a sequence of simulations in which Ri_0 was varied between 0.04 (thick solid curve) and 0.16 (thin dash-dotted curve). The latter value is close to the value 0.167 employed in the simulations of Staquet (1991, 1995).

Much of the variability due to changes in Ri_0 is simply a difference in time scales: the primary instability grows and pairs more slowly in high Ri_0 cases than in low Ri_0 cases. Increasing Ri_0 resulted in a large decrease in the maximum tilt angle. As Ri_0 is increased, the work that must be done against gravity to generate a steep tilt angle increases relative to the kinetic energy available to accomplish that work. Increasing Ri_0 also led to a slight decrease in the maximum strain rate for all except the largest value tested, $Ri_0 = 0.16$. In that case, the strain rate increased temporarily near $t = 100$, then decreased rapidly.

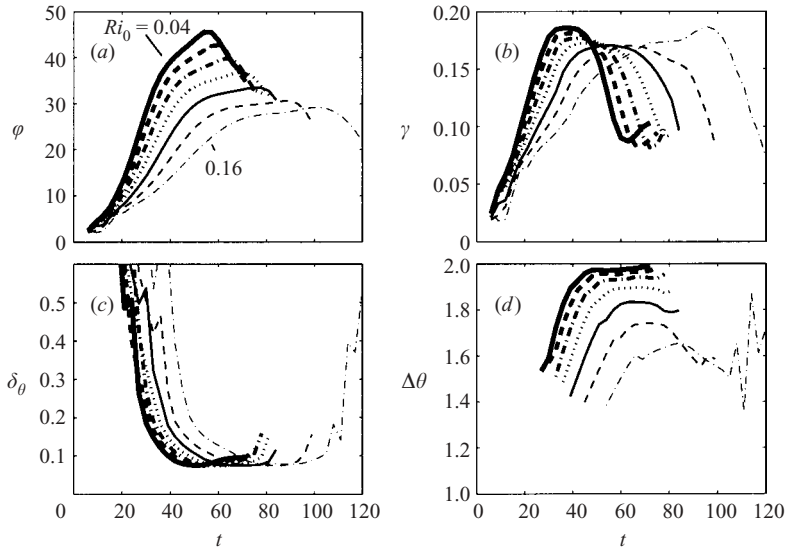

FIGURE 14. Histories of tilt angle (a), the strain rate (b), the net scalar differential (c) and the scalar thickness (d), for various values of the initial bulk Richardson number. Curve types indicate initial bulk Richardson number: thick solid curve: run #13 ($Ri_0 = 0.04$); thick dashed curve: run #14 ($Ri_0 = 0.06$); thick dash-dotted curve: run #6 ($Ri_0 = 0.08$); dotted curve: run #15 ($Ri_0 = 0.10$); thin solid curve: run #16 ($Ri_0 = 0.12$); thin dashed curve: run #17 ($Ri_0 = 0.14$); thin dash-dotted curve: run #18 ($Ri_0 = 0.16$). In all cases, $Re_0 = 2000$, $Pr = 1$.

The scalar thickness δ_θ also reflects the tendency of flows with larger Ri_0 to evolve on longer time scales (figure 14c). In each case, the thickness reached a minimum shortly after the strain reached its maximum. As predicted by the equilibrium similarity theory, this minimum value did not depend on Ri_0 (cf. equation (2.9)). The common minimum value was 0.075, which has already been shown to compare well with the predicted value (figure 11a, thick solid curve). In each case except $Ri_0 = 0.04$, the onset of secondary instability was signalled by a sharp increase in δ_θ. (In the $Ri_0 = 0.04$ case, secondary instability did not occur. Instead, the braid was engulfed by the collapsing core at about $t = 75$.) The increase in δ_θ was particularly dramatic in the case $Ri_0 = 0.16$.

The net change in the scalar field across the braid, $\Delta\theta$, is also a strong function of Ri_0 (figure 14d). The maximum possible value of $\Delta\theta$ is 2.0. At the smallest Ri_0 tested, $\Delta\theta$ increased to a value very close to this. Maximum values decreased slightly in the $Ri_0 = 0.06$ and 0.08 cases, then more dramatically with further increases in Ri_0. In the $Ri_0 = 0.12$ case, the onset of secondary instability was preceded by a slight decrease in $\Delta\theta$. This reduction was greater in the $Ri_0 = 0.14$ and 0.16 cases. In the latter case, the fitted value of $\Delta\theta$ oscillated rapidly after $t = 100$, indicating that the shape of the $\theta(z')$ profile no longer matched the theoretical prediction. This effect is also evident in the behaviour of δ_θ for the same case (figure 14c).

Figure 15 shows histories of three quantities related to secondary instability. For visual clarity, the $Ri_0 = 0.10$ and 0.14 cases have been omitted from this diagram. In the low Ri_0 cases, there is a clear inverse relationship between Ri_0 and the braid shear (figure 15a). The braid shear dropped below its equilibrium value after $t = 50$, then recovered. The inverse relationship between Ri_0 and the braid Richardson number (figure 15b) is not seen in the simulation results, except that the $Ri_0 = 0.08$ and 0.10

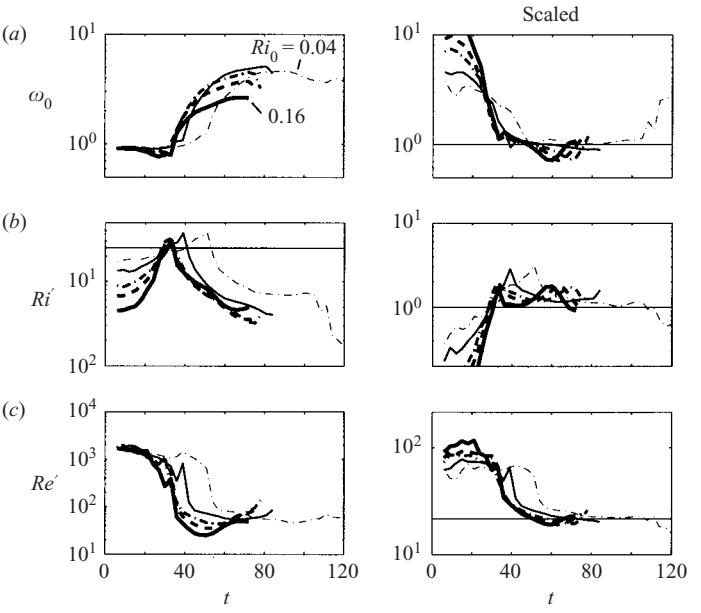

FIGURE 15. Histories of braid shear (*a*), braid Richardson number (*b*) and braid Reynolds number (*c*) for various values of the initial bulk Richardson number. Right-hand frames show the same quantities, normalized using equilibrium similarity theory. Curve types indicate initial bulk Richardson number: thick solid curve: run #13 ($Ri_0 = 0.04$); thick dashed curve: run #14 ($Ri_0 = 0.06$); thick dash-dotted curve: run #6 ($Ri_0 = 0.08$); dotted curve: run #15 ($Ri_0 = 0.10$); thin solid curve: run #16 ($Ri_0 = 0.12$); thin dashed curve: run #17 ($Ri_0 = 0.14$); thin dash-dotted curve: run #18 ($Ri_0 = 0.16$). In all cases, $Re_0 = 2000$, $Pr = 1$.

cases achieved lower Ri' values near the end of the simulations than did the $Ri_0 = 0.04$ case. The absence of the inverse relationship at higher Ri_0 may be traced back to the Ri_0 dependence of the tilt angle ϕ and the scalar differential $\Delta\theta$ (figure 14*a*, *d*), both of which tend to decrease with increasing Ri_0. Note that Ri' often exceeded its equilibrium value by 50% or more just before the onset of secondary instability. The absence of secondary instability in the $Ri_0 = 0.04$ case can also be understood in terms of the braid Reynolds number, Re' (figure 15*c*). Re' dropped to low values around $t = 50$ then recovered in all cases, but values were generally lowest in the $Ri_0 = 0.04$ case. Values of Re' agree closely with equilibrium theory in the final stages of all simulations.

As we have seen, the behaviour of the most strongly stratified case ($Ri_0 = 0.16$, thin dash-dotted curves on figure 15) was distinctive in many respects. The stable stratification was strong enough in comparison to the shear that the primary KH instability grew very slowly, and the pairing instability was strongly inhibited. From $t = 50$ to $t = 100$, the braid shear remained steady at the equilibrium value. After this time, the shear remained nearly constant, even though the equilibrium value dropped sharply due to the decrease in γ (figure 14*b*). This discrepancy with the theoretical prediction is reflected in the sharp rise of the scaled curve in the right-hand frame of figure 15(*a*) after $t = 100$. During this same interval, the braid Richardson number (figure 15*b*) dropped rapidly to values near 0.02. This decrease was due to a sudden decrease in the stratification within the braid, the reason for which will be apparent presently. Shortly after this, secondary instability appeared.

Figure 16 illustrates dramatic differences in the evolution of secondary instability as a function of initial Richardson number. Each pair of frames shows the θ-field at two

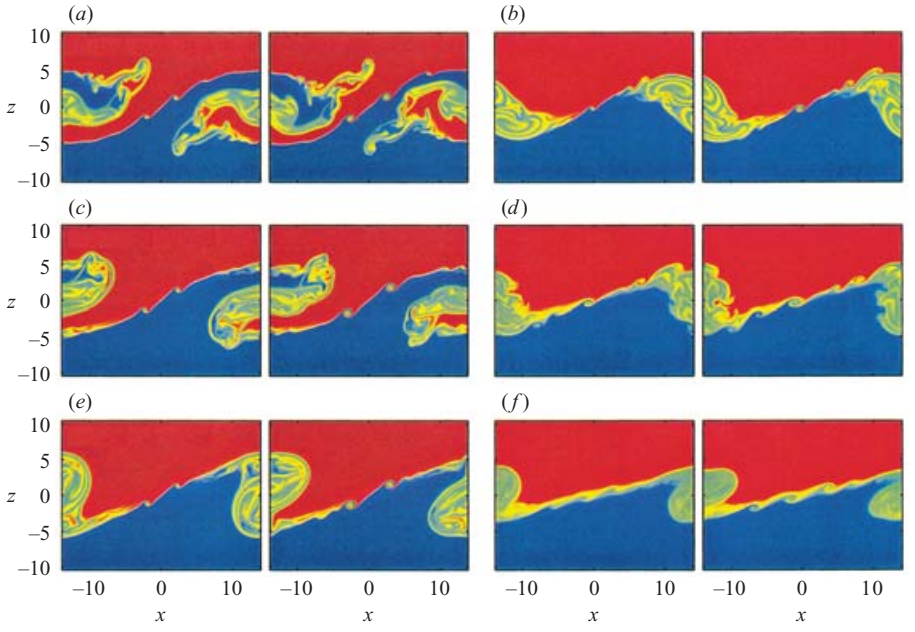

FIGURE 16. Scalar field $\theta(x, z, t)$ during the initial growth of secondary instability, for simulations (*a*) #14 ($Ri_0 = 0.06$), (*b*) #6 ($Ri_0 = 0.08$), (*c*) #15 ($Ri_0 = 0.10$), (*d*) #16 ($Ri_0 = 0.12$), (*e*) #17 ($Ri_0 = 0.14$) and (*f*) #18 ($Ri_0 = 0.16$) as labelled. In each case, $Re_0 = 2000$ and $Pr = 1$. Values of θ range from -1 (blue) to $+1$ (red).

successive times, separated by an interval of 3.0, shortly after the first appearance of secondary instability. The $Ri_0 = 0.04$ case is omitted because it did not develop secondary instability. In the $Ri_0 = 0.06$ case, a pair of secondary billows appeared on either side of the stagnation point. At the later time, the billows had grown and propagated outward away from the stagnation point. The same pattern is evident in the $Ri_0 = 0.08$ and 0.10 cases (figure 16*b*, *c*). The initial length scale of these disturbances was significantly longer than those seen at higher Re_0 (figure 10) and higher Pr (figure 13). In the $Ri_0 = 0.12$ and 0.14 cases, a single secondary billow appeared near the stagnation point, then propagated slowly to the left as it grew. This suggests the existence of two branches of secondary instability, one that generates secondary billows in pairs straddling the stagnation point, and one that creates a single billow at the stagnation point. At $Ri_0 = 0.16$, pairs of secondary billows are again evident (figure 16*f*). After about $t = 126$, four large secondary billows developed on the braid. However, they did not emerge from the stagnation point, and propagated only slowly in the x'-direction.

In most cases, secondary billows also developed in the regions where the core meets the braid. We must interpret these results with caution, however, because the outer edge of the core is a prime site for three-dimensional secondary instabilities in strongly stratified flows (Klaassen & Peltier 1991; Caulfield & Peltier 2000).

The cases shown in figure 16 also differ in the manner in which the core collapsed onto the braid. In the low Ri_0 cases, this collapse occurred all at once after the secondary billows had attained large amplitude. In the strongly stratified cases, the core did not so much collapse as spread gradually outward into the braid region. This effect was most clearly evident in the $Ri_0 = 0.16$ case, in which mixed fluid from the core (shown in yellow and light blue) had been advected along the entire length

of the braid by the time secondary instability appeared. This incursion of mixed fluid from the core into the braid explains the rapid increase in braid thickness (figure 14*d*) and the rapid decrease in braid Richardson number (figure 15*b*) in the $Ri_0 = 0.16$ case after $t = 100$. Evidently, the growth of the secondary instability was accelerated, or possibly even caused, by the influx of mixed fluid from the core. This process is also evident, though to a lesser extent, in the $Ri_0 = 0.14$ case (figure 16*e*). In the $Ri_0 = 0.12$, 0.10 and 0.08 cases (figures 16*d*, 16*c* and 16*b*), the flux of fluid from the cores was underway, but it had not yet reached the region of the secondary billows by the time they began to grow.

This incursion of fluid from the core to the braid suggests the near-core instability described by Staquet (1995). It represents a qualitative difference in the physics of the secondary instability between the low Ri_0 and high Ri_0 cases.

4. Normal-mode stability analysis

Corcos & Sherman (1976) were led to predict the existence of the secondary KH instability by the inverse dependence between braid Richardson number and Reynolds number, i.e. for sufficiently high Re_0, Ri' will always be less than 1/4 (cf. (2.21)). This reasoning is based on the well-known characteristics of inviscid non-diffusive horizontal steady shear flows (e.g. Miles 1961; Hazel 1972). Clearly, though, the braid region is more complex than this. For one thing, because of the non-zero tilt angle, the braid-parallel component of the gravitational acceleration that drives the shear across the braid must also act on any perturbation. In addition, the braid is thin enough that viscous and diffusive effects are important. (We have already examined this effect in part via the braid Reynolds number, e.g. figure 15*c*). Thirdly, the braid is not perfectly steady, but rather is part of an evolving flow. Finally, the braid is subject to a strong straining deformation. All of these effects except for the last two can be incorporated into a normal-mode stability analysis. Away from stability boundaries, the time dependence of the braid is unlikely to affect the results significantly as it is slow compared with the rate at which secondary KH instabilities grow. In contrast, the neglect of strain is a serious shortcoming. These caveats notwithstanding, the normal-mode model represents a significant refinement of previous ideas based on consideration of the Richardson number alone. In this section, I will assess the degree to which normal-mode stability theory can describe the secondary KH instability.

The analysis begins with the identification of the equilibrium flow, whose stability is to be tested, with the braid-perpendicular profiles defined in § 2.4: $U = u'(z')$; $\Theta = \theta(z')$. The braid-perpendicular velocity w' is ignored. I then assume that the flow consists of these profiles plus a small perturbation having the normal-mode form

$$\left.\begin{aligned} \theta(x', z', t) &= \hat{\theta}(z')\, \mathrm{e}^{\sigma t + \mathrm{i}kx'}, \\ \omega(x', z', t) &= \hat{\omega}(z')\, \mathrm{e}^{\sigma t + \mathrm{i}kx'}, \end{aligned}\right\} \tag{4.1}$$

in which k is a real non-dimensional wavenumber, σ is the corresponding complex growth rate, $\hat{\theta}$ and $\hat{\omega}$ are complex functions of z' and only the real parts of the right-hand sides are physically relevant. This normal-mode solution is consistent with the assumptions of stationarity and homogeneity in x' that underlie the equilibrium similarity theory, the validity of which was assessed in § 3. Substituting these expressions into (2.5) and ignoring products of perturbation quantities leads to

$$\begin{bmatrix} A_{11} & A_{12} \\ A_{21} & A_{22} \end{bmatrix} \begin{pmatrix} \hat{\omega} \\ \hat{\theta} \end{pmatrix} = \sigma \begin{pmatrix} \hat{\omega} \\ \hat{\theta} \end{pmatrix} \tag{4.2}$$

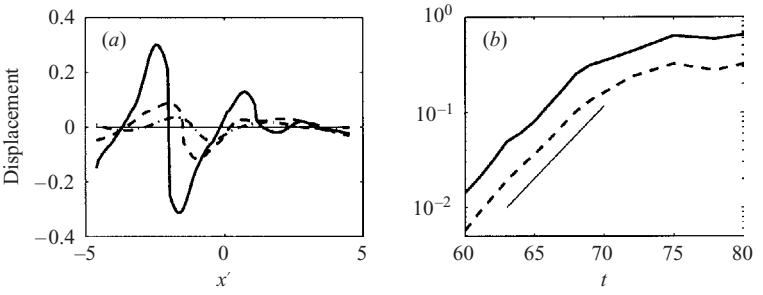

FIGURE 17. Growth of the initial secondary billow in run #7. (*a*) Perpendicular displacement of the braid centre $z_b(x)$ from the cubic fit $z_f(x)$ at $t=63$ (dash-dotted curve), $t=66$ (dashed curve) and $t=69$ (solid curve). (*b*) Maximum absolute displacement (solid curve) and root-mean-square displacement (dashed) as functions of time. The straight line corresponds to an exponential growth rate of 0.35.

where the elements of the array $\boldsymbol{A}$ are the following ordinary differential operators:

$$\left.\begin{aligned} A_{11} &= -\mathrm{i}kU + \mathrm{i}k\frac{\mathrm{d}^2U}{\mathrm{d}z'^2}\nabla^{-2} + \frac{1}{Re_0}\nabla^2, \quad A_{12} = Ri_0(\mathrm{i}k\cos\varphi + \sin\varphi\,\partial_{z'}), \\ A_{21} &= -\mathrm{i}kRi_0\frac{\mathrm{d}\Theta}{\mathrm{d}z'}\nabla^{-2}, \quad A_{22} = -\mathrm{i}kU + \frac{1}{Re_0Pr}\nabla^2. \end{aligned}\right\} \tag{4.3}$$

The operator ∇^{-2} represents the inverse of the Laplacian $\mathrm{d}^2/\mathrm{d}z'^2 - k^2$ subject to homogeneous Dirichlet conditions at boundaries located far enough from the braid to have no significant effect. Discretizing the z'-dependence using fourth-order compact derivatives (Lele 1992) converts (4.2) into an algebraic matrix equation that can be solved using standard methods. The result is the dispersion equation $\sigma = \sigma(k; Re, Pr, Ri, \varphi, U, \Theta)$. For a given set of profiles and parameter values, the fastest-growing mode (FGM) is the mode that maximizes the real part of σ as a function of k. For all cases considered here, σ is purely real.

Although this analysis cannot include the effects of strain explicitly, those effects can be accounted for after the fact in a non-rigorous but intuitively appealing way. Advection by the extensional strain is expected to increase the wavelength of any disturbance, and thus to decrease k, exponentially at rate γ. Instability causes disturbances to expand exponentially in the braid-perpendicular direction at rate σ, while the strain acts to compress disturbances in the same direction at rate γ. The net growth rate is therefore estimated as $\sigma - \gamma$ (Staquet 1991).

Quantitative comparison of the wavenumber and growth rate predicted using normal-mode stability analysis with the corresponding properties of secondary billows is non-trivial, owing to the difficulty of defining those properties for a billow growing on a complex evolving background flow. Figure 17(*a*) shows the amplitude of the secondary instability at selected times during run #7. This amplitude is calculated as the perpendicular displacement between the braid centre z_b and the cubic fit z_f as described in § 2.4. At each of the three times shown, a prominent wave-like disturbance is visible to the left of the stagnation point $x'=0$. This disturbance corresponds to the early form of the secondary billow visible near $x=-5$ in figure 10. Closer inspection shows that the length scale of the disturbance is about 3.6, so the wavenumber is about 1.8. As shown in figure 17(*b*), this disturbance grew exponentially with growth rate 0.35.

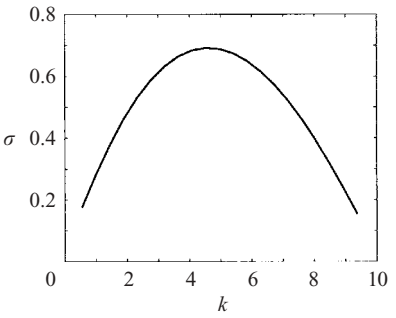

FIGURE 18. Normal-mode dispersion relation for the braid in simulation #7 at $t = 66$.

Figure 18 shows the dispersion relation $\sigma(k)$ computed for this flow at $t = 66$. The FGM had wavenumber $k = 4.6$ and growth rate $\sigma = 0.69$. Evidently, the measured disturbance exhibits both smaller wavenumber and slower growth than the FGM. These discrepancies, however, are what we would expect as a result of the strain. At $t = 66$, the strain rate was $\gamma = 0.11$. If the wavenumber were decreasing exponentially at this rate, it would require a time interval of 9 to decrease to the measured value of 1.8. This is consistent with the time scale over which the secondary billow appears to have grown. (On the other hand, no such growth is evident over the interval shown in figure 17.) At $k = 1.8$, the predicted growth rate from the normal-mode analysis (figure 18) is 0.44. If we assume that the net effect of the strain is to reduce the growth rate by an amount γ, then we would expect a net growth rate of 0.33. This compares quite favourably with the growth rate 0.35 obtained empirically from the simulation. This comparison has been made for other cases with similar results. The length scale of the secondary billows tends to be longer than that of the FGM by an amount that is broadly consistent with exponential spreading by the strain field, while the growth rate matches to within a few tens of percent after the theoretical value σ for the observed wavenumber is reduced to $\sigma - \gamma$.

The top row of figure 19 shows the predicted growth rate $\sigma - \gamma$ of the FGM as a function of time for most of the simulations discussed previously. (Because γ is generally much smaller than σ, the behaviour of σ is not much different from that of $\sigma - \gamma$, so I have only shown the latter. Also note that the strain-induced decrease of the wavenumber is not considered in this calculation.) The growth rate increases strongly with increasing Reynolds number (figure 19*a*), and maximum growth rates also occur earlier in the high Re_0 cases. This corresponds to the early appearance of secondary instability in those cases (cf. figure 9*a*, right-hand frame). The $Re_0 = 1000$ case (solid curve) attained a much lower maximum growth rate than did the other cases, and it did not produce secondary instability until the end of the simulation (figure 5*c*). Increasing Prandtl number (figure 19*b*) has a more subtle effect: there is no systematic increase in the maximum growth rate with Pr, but that maximum does occur significantly earlier in the high Pr cases. This is consistent with the simulation results described in § 3.3. As was found in § 3.4, the influence of the bulk Richardson number Ri_0 is complicated due to its order-zero effects on the primary instability (figure 19*c*). In general, the higher Ri_0 cases take longer to attain maximum growth rate. The largest growth rate occurs at $t = 57$ for the case $Ri_0 = 0.10$ (dotted curve). The $Ri_0 = 0.04$ case (thick solid curve) attained a much lower maximum growth rate than did the other flows, and it failed, correspondingly, to develop secondary

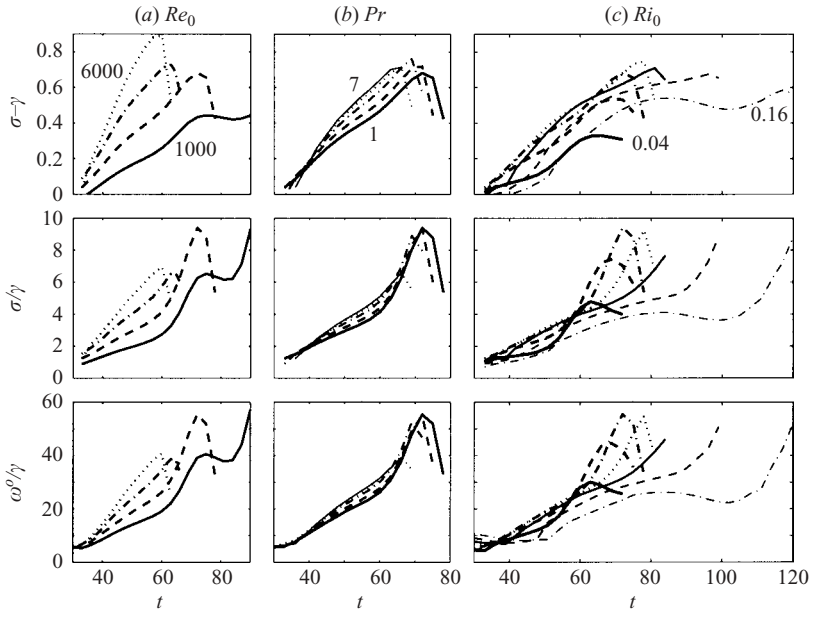

FIGURE 19. Top row: predicted growth rate $\sigma - \gamma$ of the fastest growing mode of the braid, considered as a parallel shear flow in equilibrium, at various times during the evolution of the primary KH instability. The parameter varied is indicated at the top; labels in the upper frames indicate extremal values. Second row: ratio of growth rate σ to strain rate γ. Bottom row: ratio of braid shear ω^o to strain rate. (*a*) Curve types are as given in the caption to figure 9. (*b*) Curve types are as given in the caption to figure 12. (*c*) Curve types are as given in the caption to figure 14.

instability. The $Ri_0 = 0.16$ case attained a temporary maximum in $\sigma - \gamma$ at $t = 80$, but it did not develop secondary billows until $\sigma - \gamma$ increased again after $t = 100$.

The second row of figure 19 gives the ratio σ/γ. This ratio is a likely candidate to be the basis of an empirical criterion for secondary instability. The only case that never developed secondary instability (figure 19*c*, solid curve) also never attained a value greater than 5 for this ratio. In all other cases, instability developed shortly after σ/γ passed the value 6. Both the two highest Reynolds number cases (figure 19*a*, dotted and dash-dotted curves) and the two highest Prandtl number cases (figure 19*b*, dotted and thin solid curves) exhibited secondary instability after just barely attaining this value. (Note that these flows attain maximum σ early in the pairing process, while the strain field is still at its maximum. Thus, the ratio σ/γ is relatively small despite the large values of σ predicted for these cases.) In contrast, the low Re_0 case (figure 19*a*, solid curve) remained stable after achieving a value of 6.5 (near $t = 75$), and developed instability only after σ/γ reached much higher values near the end of the simulation as the braid was being engulfed by the core (cf. figure 5*c*).

The bottom row of figure 19 shows the ratio of braid shear to strain, i.e. ω_0/γ, the basis of the empirical criterion for instability proposed by Staquet (1995). Remarkably, this ratio was very nearly proportional to σ/γ in all cases, indicating that the normal-mode growth rate is nearly proportional to the shear despite the effects of stratification, viscosity, diffusion and braid tilt, all of which acts to upset this proportionality. Staquet (1995) proposed the critical value 54 for this ratio. The present results suggest that a value in the range 35–40 is sufficient to produce secondary instability.

Ultimately, the Staquet criterion is of superior utility because it can be evaluated without the need for the normal-mode stability analysis. Both criteria give incomplete descriptions of the physics of secondary instability though, as is clear from the fact that they are well satisfied for the $Re = 1000$ case (figure 19*a*, thick solid curve) long before instability appears and, conversely, the high Reynolds and Prantdl number cases develop robust instability after satisfying the criteria only marginally.

5. The efficiency of mixing

In practical applications, mixing efficiency is a crucial property of any turbulent (or preturbulent) flow. The extraordinary mixing efficiency of preturbulent KH billows (e.g. Winters *et al.* 1995; Smyth *et al.* 2001) is the main motivation for examining the physics of such flows at the present level of detail. While a comprehensive view of mixing must await three-dimensional direct simulations at high Re_0, the present results are sufficient to indicate the essential effect (i.e. increase or decrease) of secondary instability on mixing efficiency.

Because the energetics of mixing in stratified flow is complicated by gravity waves, it is standard to quantify mixing efficiency using the flux coefficient, Γ, which is the ratio of irreversible potential energy gain to kinetic energy dissipation. Following Winters *et al.* (1995), I define the background potential energy, P_b, as the minimum potential energy achievable via adiabatic reordering of fluid parcels. (In practice, this reordering is accomplished by a simple sorting of the θ-array.) After this reordering, the fluid parcel located originally at (x, z) will have vertical coordinate $z^*(x, z)$. The background potential energy is then given by

$$P_b = -Ri_0 \int \theta z^* \, \mathrm{d}x \, \mathrm{d}z, \tag{5.1}$$

where the integral is taken over the computational domain. The rate of increase of P_b due to mixing may be written as

$$\frac{\mathrm{d}P_b}{\mathrm{d}t} = \int \frac{Ri_0}{Re_0 Pr} \nabla\theta \cdot \nabla z^* \, \mathrm{d}x \, \mathrm{d}z. \tag{5.2}$$

(Equation (5.2) is obtained from equation (14) of Winters *et al.* (1995) using a standard vector identity and neglecting changes in P_b due to boundary fluxes.) The rate at which kinetic energy is dissipated via friction is given by

$$\epsilon = \int \frac{1}{Re_0} [4(\partial u/\partial x)^2 + (\partial u/\partial z + \partial w/\partial x)^2] \, \mathrm{d}x \, \mathrm{d}x, \tag{5.3}$$

and the flux coefficient is then

$$\Gamma = \frac{\mathrm{d}P_b/\mathrm{d}t}{\epsilon}. \tag{5.4}$$

Ideally, this computation is done on fully three-dimensional flow fields. In the present study, the artifice of two-dimensionality has been adopted in order to gain access to higher Reynolds number flows. The main cost of this artifice is a loss of accuracy in the cores, where three-dimensional motions would develop rapidly were they not suppressed. When assessing the effect of secondary instability on mixing efficiency, the computations must be arranged so as to minimize this loss of accuracy. I do this by defining a time-dependent subset B of the computational domain to represent the braids, and performing the integrals in (5.2) and (5.3) over that area only. (There will still be an influence from the cores via the computation of z^*, but it

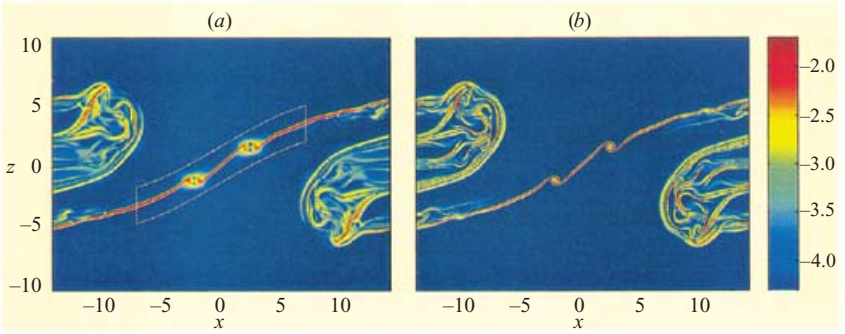

FIGURE 20. (*a*) Local dissipation rate, computed as the integrand of (5.3), for run #6 at $t = 81$. Solid curves indicate the boundaries of the braid sample region, B. (*b*) Local contribution to the irreversible potential energy gain, computed as the integrand of (5.2), for the same flow. Values on the scale denote the common logarithm of either field.

is expected to be small.) B is defined as the area $|z - z_f(x)| < 1.5$, where z_f is the cubic approximation to the braid defined as in (2.22). For the present purpose, the braid sample is extended from $-L_x/4$ to $L_x/4$. Figure 20 shows the local dissipation rate $[4(\partial u/\partial x)^2 + (\partial u/\partial z + \partial w/\partial x)^2]/Re_0$ and the local contribution to the irreversible potential energy gain $\nabla\theta \cdot \nabla z^* Ri_0/Re_0 Pr$ for a representative case. Both quantities exhibit highly compact spatial support. The braid region B is delineated by the solid curves on figure 20(*a*).

Figure 21 shows histories of $\mathrm{d}P_b/\mathrm{d}t$, ϵ and Γ for the sequence of runs described in § 3.2. For each case, $Ri_0 = 0.08$ and $Pr = 1$. Reynolds numbers range from 1000 (solid curve) to 6000 (dotted curve). During the initial growth and pairing of the primary KH instability, irreversible potential energy gain (figure 21*a*) was greatest for low Re_0. The same is true of the kinetic energy dissipation rate (figure 21*b*). To interpret this result properly, we must keep in mind that all quantities are non-dimensionalized using the same length and velocity scales that define the Reynolds number; thus, varying Re_0 is best thought of as equivalent to varying the viscosity. It is therefore not surprising that the low Re_0 (most viscous) cases mix most rapidly in this scaling.

Shortly after $t = 60$, the $Re_0 = 6000$ case exhibited a rapid increase in $\mathrm{d}P_b/\mathrm{d}t$. This time corresponds to the onset of secondary instability. Comparable increases in $\mathrm{d}P_b/\mathrm{d}t$ occurred at later times in the $Re_0 = 4000$ and $Re_0 = 2000$ cases, but not in the $Re_0 = 1000$ case (for which secondary instability did not occur until just before the braids were engulfed by the collapsing core). During the same time period, the dissipation rate showed no such increase, but instead decreased in every case. These results suggest that onset of secondary instability was accompanied by a rapid acceleration of irreversible potential energy gain and a moderate slowing of viscous dissipation.

The effect of secondary instability is expressed very clearly in the evolution of the flux coefficient, Γ (figure 21*c*). Γ was nearly independent of Reynolds number during the initial growth and pairing phases, but increased dramatically as secondary instability appeared in the $Re_0 = 6000$, 4000 and 2000 cases in turn.

Mixing efficiency is known to be a strong function of the Prandtl number (e.g. Smyth *et al.* 2001). This is reflected in the dependence of $\Gamma(t)$ on Pr shown in figure 22. Just prior to the onset of secondary instability, values range from 2.0 in the $Pr = 1$ case down to 0.5 in the $Pr = 7$ case. These values are consistent with the results obtained by Smyth *et al.* (2001) in three-dimensional simulations over the same range

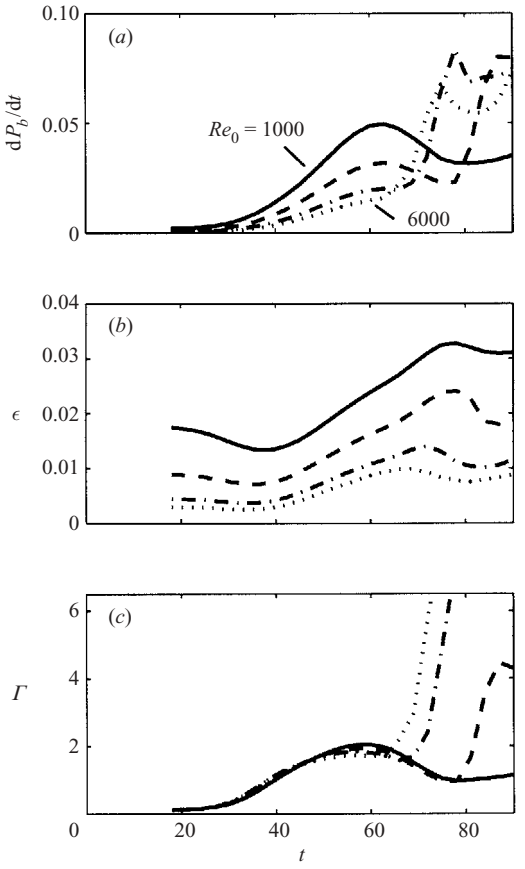

FIGURE 21. (*a*) Rate of irreversible potential energy increase, (*b*) rate of kinetic energy dissipation and (*c*) the ratio Γ. Only contributions from the braid region B are included. Curve types indicate initial Reynolds number: thick solid curve: run #1 ($Re_0 = 1000$); dashed curve: run #6 ($Re_0 = 2000$); dash-dotted curve: run #7 ($Re_0 = 4000$); dotted curve: run #8 ($Re_0 = 6000$). In all cases, $Ri_0 = 0.08$, $Pr = 1$.

of Pr (cf. figure 12 of that paper). The three-dimensional simulations were at lower Reynolds number, but we know that Γ is insensitive to Re_0 in this flow regime. The essential difference between the present simulations and those of Smyth *et al.* (2001) is the dimensionality, and the correspondence noted here indicates that the essential physics of the braid region is accurately represented in our two-dimensional model. This correspondence with lower Reynolds number results ends abruptly with the onset of secondary instability, which precipitates a dramatic increase of Γ in each case. Because secondary instability appears earliest in the high Pr cases, those flows soon exhibit Γ values close to those of the lower Pr cases. At $t = 75$, the $Pr = 7$ case actually exhibits the highest mixing efficiency. Subsequently, values of Γ increase into the range 2.5–4.5 in all cases.

The dependence of $\Gamma(t)$ on the initial bulk Richardson number is shown in figure 23. In the $Ri_0 = 0.04$ case, the braid was engulfed by the collapsing core near $t = 75$, before secondary instability could develop. In all other cases, secondary instability led to a rapid increase in $\Gamma(t)$. The most rapid increases occurred in the $Ri_0 = 0.08$ and 0.10 cases.

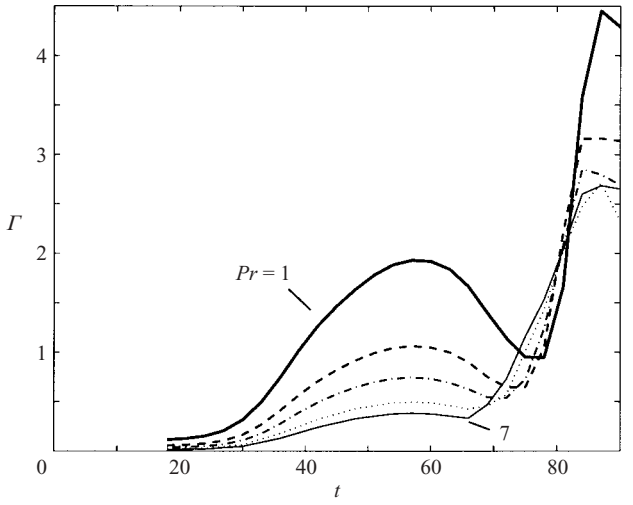

FIGURE 22. Evolution of Γ for various Pr. Only contributions from the braid region B are included. Thick solid curve: run #6 ($Pr = 1$); dashed curve: run #9 ($Pr = 2$); dash-dotted curve: run #10 ($Pr = 3$); dotted curve: run #11 ($Pr = 5$); thin solid curve: run #12 ($Pr = 7$). In all cases, $Ri_0 = 0.08$, $Re_0 = 2000$.

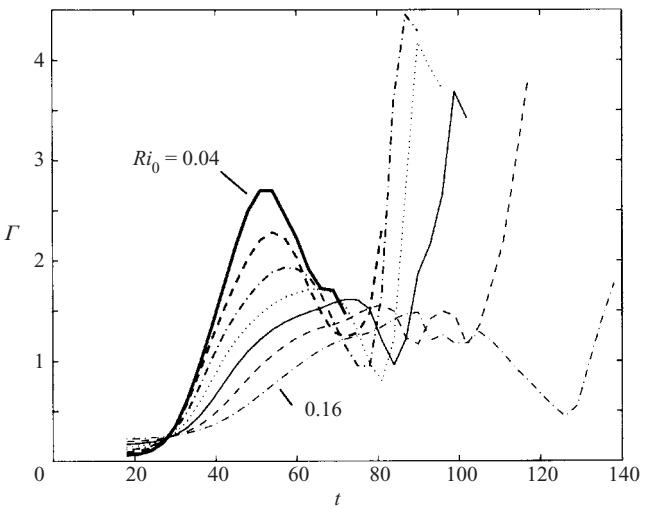

FIGURE 23. Evolution of Γ for various Ri. Only contributions from the braid region B are included. Curve types indicate initial bulk Richardson number: thick solid curve: run #13 ($Ri_0 = 0.04$); thick dashed curve: run #14 ($Ri_0 = 0.06$); dash-dotted curve: run #6 ($Ri_0 = 0.08$); dotted curve: run #15 ($Ri_0 = 0.10$); thin solid curve: run #16 ($Ri_0 = 0.12$); thin dashed curve: run #17 ($Ri_0 = 0.14$); thin dash-dotted curve: run #18 ($Ri_0 = 0.16$). In all cases, $Re_0 = 2000$, $Pr = 1$.

It must be emphasized that these results are approximate and pertain to the braid region only. The high values of Γ seen here might not be reproduced if the computation were done over the entire domain of a three-dimensional flow. Nevertheless, the present results do suggest strongly that the effect of secondary instability is to increase mixing efficiency.

6. Discussion

I have described two-dimensional simulations of merging KH billows, focusing the analysis on the initial growth of secondary KH instability on the braids. This work extends the results of Staquet (1995) to lower bulk Richardson numbers ($0.04 \leqslant Ri_0 \leqslant 0.16$) and higher Prandtl numbers ($1 \leqslant Pr \leqslant 7$). The secondary instability appears over most of this parameter range when the Reynolds number exceeds ~ 1000. I have also extended the equilibrium similarity theory of Corcos & Sherman (1976) to Prandtl numbers greater than unity, and have shown that the theory provides a useful description of the physics of the braid just prior to the onset of secondary instability.

As predicted by Corcos & Sherman (1976), the tendency towards secondary instability increases strongly with increasing Reynolds number. This is due mainly to that fact that the strain field is able to compress the braid more effectively, leading to a stronger shear across the braid. Increasing Prandtl number has a similar effect, albeit less pronounced. (According to the equilibrium theory, the shear across the braid is proportional to $Re_0^{0.50}$ and to $Pr^{0.13}$, cf. (2.17).) Increasing Pr decreases the scalar thickness of the braid directly, and the vorticity thickness indirectly by decreasing the length scale over which the baroclinic torque acts.

The effects of varying the initial bulk Richardson number are complicated because Ri_0 also has an order-zero effect on the primary KH instability. At sufficiently low Ri_0, secondary instability is weak and the braid is engulfed by the collapsing core before secondary billows can develop. In the limit $Ri_0 \to 0$, the baroclinic torque that drives the braid shear is absent, and secondary instability is rarely observed (Dritschel *et al.* 1991). For Ri_0 greater than about 0.12 (including the value 0.167 studied by Staquet (1995)), secondary instability is influenced by a flux of mixed fluid from the core onto the braid.

For Ri_0 in the range 0.06–0.12, secondary instability is not affected by the collapsing core, i.e. it is governed solely by the local properties of the braid. Secondary billows may be created either singly or in pairs straddling the stagnation point. The evolution of billows created in pairs appears to depend upon a competition between the extensional strain and the pairing instability (e.g. Klaassen & Peltier 1989). The former effect advects the secondary billows outward away from the stagnation point, while the latter merges them into a single stationary billow. In most cases studied here, the former effect dominated, i.e. pairs of billows propagated outward as they grew, but in the example shown in figure 10, the two innermost secondary billows subsequently merged and remained at the stagnation point. The causes of this multiplicity of behaviours, and the regions of parameter space in which each dominates, remain to be explored.

Atsavapranee & Gharib (1997) documented secondary KH billows in laboratory experiments using the tilted tube technique of Thorpe (1968). Estimated values of the bulk Richardson number for cases in which secondary billows appeared were 0.043 and 0.026 (their figures 8 and 11, respectively). The initial Reynolds number was defined using the full thickness, not the half-thickness, of the shear layer, resulting in values for Re_0 around 2000. For comparison with the present results, however, the appropriate value is based on the half-thickness and is therefore ~ 500. While these parameter values are all below the ranges in which I have found secondary billows in the present work, the Prandtl (or Schmidt) number in the experiments was 600, much higher than the highest value attained here. The high Prandtl number may have compensated for the suboptimal Richardson and Reynolds numbers. More extensive laboratory explorations of the parameter space in which

secondary KH instabilities appear could add greatly to our understanding of this instability.

Mixing efficiency has been examined via Γ, the ratio of irreversible potential energy gain to energy lost to friction, and has been found to be highly sensitive to the appearance of secondary instability. In every example, the onset of secondary instability was accompanied by a dramatic increase in Γ.

The mixing efficiencies computed prior to the onset of secondary instability agree with those obtained from three-dimensional simulations at the same *Pr* (Smyth *et al.* 2001), suggesting that the assumption of two-dimensionality is valid for the braid region, at least. However, I have regarded the small-scale details of flow in the core as suspect, and this has precluded the assessment of instability and mixing in that region. Even in the braids, the secondary KH instability must compete with braid-centred three-dimensional instabilities (e.g. Klaassen & Peltier 1991; Cortesi *et al.* 1998) in a manner that has not yet been explored. Moreover, the secondary KH instabilities are themselves expected to become three-dimensional upon reaching large amplitude. Therefore, a full understanding of the significance of secondary instability in real mixing events must await the availability of three-dimensional direct simulations with Reynolds numbers of order 1000 or higher. Computing technology is now approaching the stage where such simulations are possible, particularly in the low Prandtl number regime (e.g. Winters *et al.* 2003).

A theoretical description of the secondary KH instability is probably best obtained via non-separable stability analysis of the two-dimensional flow (e.g. Klaassen & Peltier 1989). Unfortunately, such calculations make extreme demands on computational resources. Both the memory and the processing time needed are proportional to the squares of the corresponding requirements for two-dimensional simulations with the same spatial resolution. To carry out a non-separable analysis with a triangular wavenumber truncation (Klaassen & Peltier 1989; Smyth & Peltier 1993), using the minimum acceptable resolution identified in § 3.1, would require finding eigenvalues and eigenvectors of a $10^5 \times 10^5$ complex general matrix! Such a computation is prohibitively expensive at the present time. Calculations with reduced resolution sufficient to capture only the main features of the secondary instability are probably feasible, but still represent a major computational challenge.

A more accessible approach is to treat the braid as a stationary parallel shear layer and perform a standard normal-mode stability analysis, as was done in § 4. This analysis quantifies the competition between braid shear and stratification, and is readily extended to include the effects of viscosity, diffusion and braid tilt on the growth of the secondary instability. Unfortunately, the normal-mode assumption demands that the strain be neglected, as its inclusion renders the problem non-separable. The results are approximately consistent with the empirically determined behaviour of the secondary billows, but only after application of an *ad hoc* correction for strain effects. An empirical criterion for instability based on the normal-mode growth rate delivers no appreciable improvement over the simpler criterion proposed by Staquet (1995) using the braid shear. These results indicate that strain effects are both highly complex and integral to the physics of the secondary instability. The presence of strain renders the secondary KH instability a much richer physical phenomenon than its primary counterpart. Its theoretical description presents an appealing challenge for the future.

This work has benefited from discussions with Renellys Perez, Steve Thorpe, Jonathan Nash, Jody Klymak, Jim Moum, Alexander Perlin and Alan Barton, and

from the comments of two anonymous reviewers. The research was funded by the National Science Foundation under grant OCE0095640.

REFERENCES

Atsavapranee, P. & Gharib, M. 1997 Structures in stratified plane mixing layers and the effects of cross-shear. *J. Fluid Mech.* **342**, 53–86.

Caulfield, C. & Peltier, W. 1994 Three-dimensionalization of the stratified mixing layer. *Phys. Fluids* **6**, 3803–3805.

Caulfield, C. & Peltier, W. 2000 Anatomy of the mixing transition in homogeneous and stratified free shear layers. *J. Fluid Mech.* **413**, 1–47.

Corcos, G. & Sherman, F. 1976 Vorticity concentration and the dynamics of unstable free shear layers. *J. Fluid Mech.* **73**, 241–264.

Cortesi, A., Smith, B., Yadigaroglu, G. & Banerjee, S. 1999 Numerical investigation of the entrainment and mixing processes in neutral and stably-stratified mixing layers. *Phys. Fluids* **11**, 162–185.

Cortesi, A., Yadigaroglu, G. & Banerjee, S. 1998 Numerical investigation of the formation of three-dimensional structures in stably-stratified mixing layers. *Phys. Fluids* **10**, 1449–1473.

Dritschel, D., Haynes, P., Juckes, M. & Shepherd, T. 1991 The stability of a two-dimensional vorticity filament under uniform strain. *J. Fluid Mech.* **230**, 647–665.

Hazel, P. 1972 Numerical studies of the stability of inviscid parallel shear flows. *J. Fluid Mech.* **51**, 39–62.

Howard, L. 1961 Note on a paper of John W. Miles. *J. Fluid Mech.* **10**, 509–512.

Kelvin, Lord 1871 Hydrokinetic solutions and observations. *Phil. Mag.* **10**, 155–168.

Klaassen, G. & Peltier, W. 1989 The role of transverse secondary instabilities in the evolution of free shear layers. *J. Fluid Mech.* **202**, 367–402.

Klaassen, G. & Peltier, W. 1991 The influence of stratification on secondary instability in free shear layers. *J. Fluid Mech.* **227**, 71–106.

Lele, S. 1992 Compact finite difference schemes with spectral-like resolution. *J. Comput. Phys.* **103**, 16–42.

Miles, J. 1961 On the stability of heterogeneous shear flows. *J. Fluid Mech.* **10**, 496–508.

Patnaik, P., Sherman, F. & Corcos, G. 1976 A numerical simulation of Kelvin-Helmholtz waves of finite amplitude. *J. Fluid Mech.* **73**, 215–240.

Peltier, W., Halle, J. & Clark, T. 1978 The evolution of finite-amplitude Kelvin-Helmholtz billows. *Geophys. Astrophys. Fluid Dyn.* **10**, 53–87.

Press, W., Teukolsky, S., Vetterling, W. & Flannery, B. 1992 *Numerical Recipes in Fortran: The Art of Scientific Computing*, 2nd edn. Cambridge University Press.

Smyth, W. 1999 Dissipation range geometry and scalar spectra in sheared, stratified turbulence. *J. Fluid Mech.* **401**, 209–242.

Smyth, W. & Moum, J. 2000*a* Anisotropy of turbulence in stably stratified mixing layers. *Phys. Fluids* **12**, 1343–1362.

Smyth, W. & Moum, J. 2000*b* Length scales of turbulence in stably stratified mixing layers. *Phys. Fluids* **12**, 1327–1342.

Smyth, W., Moum, J. & Caldwell, D. 2001 The efficiency of mixing in turbulent patches: inferences from direct simulations and microstructure observations. *J. Phys. Oceanogr.* **31**, 1969–1992.

Smyth, W. & Peltier, W. 1993 Two-dimensional turbulence in homogeneous and stratified shear layers. *Geophys. Astrophys. Fluid Dyn.* **69**, 1–32.

Staquet, C. 1991 Influence of a shear on a stably stratified flow. In *Turbulence and Coherent Structures* (ed. O. Metais & M. Lesieur), pp. 469–487. Kluwer.

Staquet, C. 1995 Two-dimensional secondary instabilities in a strongly stratified shear layer. *J. Fluid Mech.* **296**, 73–126.

Staquet, C. 2000 Mixing in a stably stratified shear layer: two- and three-dimensional numerical experiments. *Fluid. Dyn. Res.* **27**, 367–404.

Staquet, C. & Bouruet-Aubertot, P. 2001 Mixing in weakly turbulent stably stratified flows. *Dyn. Atmos. Oceans* **34**, 81–102.

Thorpe, S. 1968 A method of producing a shear flow in a stratified fluid. *J. Fluid Mech.* **32**, 693–704.

Thorpe, S. 1981 An experimental study of critical layers. *J. Fluid Mech.* **103**, 321–344.

Thorpe, S. 1987 Transition phenomena and the development of turbulence in stratified fluids. *J. Geophys. Res.* **92**, 5231–5245.

Winters, K., Lombard, P., Riley, J. & D'Asaro, E. A. 1995 Available potential energy and mixing in density-stratified fluids. *J. Fluid Mech.* **289**, 115–128.

Winters, K., MacKinnon, J. & Mills, B. 2003 A spectral model for process studies of rotating, density-stratified flows. *J. Atmos. Ocean. Technol.* (in press).

Woods, J. 1969 On Richardson's number as a criterion for laminar-turbulent-laminar transition in the ocean and atmosphere. *Radio Sci.* **4**, 1289–1298.